The influence of uncertain local subsoil conditions on the response of buildings to ground vibration ☆,☆☆

Manthos Papadopoulos*, Stijn François, Geert Degrande, Geert Lombaert

[a]*KU Leuven, Department of Civil Engineering, Kasteelpark Arenberg 40 - box 2448, 3001 Leuven, Belgium*

Abstract

This paper examines the influence of imperfect knowledge of the local subsoil conditions on the prediction of building response to ground-borne vibration. The focus is on problems of environmental ground vibration in the wide frequency range between 1 Hz and 80 Hz. A probabilistic finite element-perfectly matched layers model is developed for the analysis of the dynamic soil-structure interaction problem where the shear modulus of the soil is modeled as a conditional random field. A subdomain formulation is employed to impose loading by an incident wave field in the model. The uncertainty on the subsoil properties is propagated to the response of a building by means of Monte Carlo simulation. A case study is considered to investigate the influence of the spatial correlation length of the random field representing the shear modulus of the subsoil, and the foundation type of the building. The structural response uncertainty varies over frequency bands but as a general trend increases with frequency. The foundation type of the building is a crucial parameter determining the structural response and the associated uncertainty bounds.

Keywords: ground-borne vibration, dynamic soil-structure interaction, elastic wave propagation, random elastic media, perfectly matched layers, Monte-Carlo simulation

1. Introduction

In the built environment, environmental ground vibration is produced by sources such as road and railway traffic or construction and industrial activities. The passage of vehicles over uneven roads or tracks and the operation of heavy machinery generate elastodynamic waves that propagate through the soil and impinge on the foundation of nearby structures leading to structural vibrations. These vibrations may lead to malfunctioning of sensitive equipment, discomfort of people, and, at very high levels, structural damage. Furthermore, noise can be re-radiated from floors and walls.

Dynamic soil-structure interaction (SSI) plays a crucial role in the prediction of the response of buildings to ground-borne vibration. Studies on dynamic SSI initiated in the field of earthquake

☆ *Postprint submitted to Journal of Sound and Vibration*

☆☆ *Published version:* M. Papadopoulos, S. François, G. Degrande, G. Lombaert. The influence of uncertain local subsoil conditions on the response of buildings to ground vibration. *Journal of Sound and Vibration*, 418:200–220, 2018. https://doi.org/10.1016/j.jsv.2017.12.021

*Corresponding author. Tel.: + 32 (0) 16 32 21 97.

Email address: manthos.papadopoulos@kuleuven.be (Manthos Papadopoulos)

engineering for the design and construction of structures of high importance such as nuclear power plants, arch dams and long-span bridges [1, 2, 3]. More recently, the growing traffic volume, the development of high-speed railway lines, and the expansion of underground transportation networks in densely populated urban areas (figure 1) have led to an interest in the problem for environmental vibration where computational models have been developed for both the prediction of the induced incident wave field and the structural response [4, 5, 6].

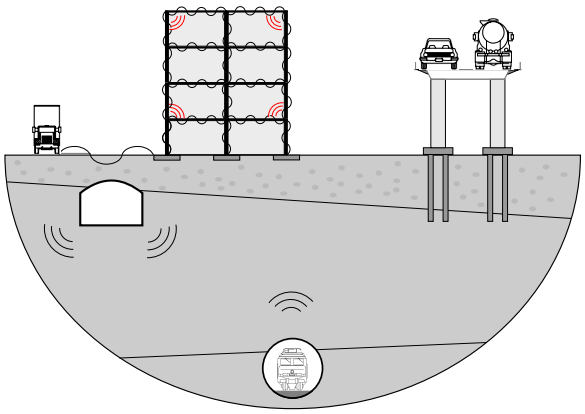

Figure 1: Traffic induced vibrations in the built environment.

In these computational models, the semi-infinite extent of the soil needs to be taken into account by allowing the radiation of elastodynamic waves to infinity. At present, this is achieved by using either coupled finite element (FE)-boundary element (BE) formulations [7] or finite element formulations in conjunction with appropriate absorbing boundary conditions (ABC) [8, 9] or perfectly matched layers (PML) [10, 11, 12]. In FE-BE formulations, a subdomain approach is followed [2, 13] where finite elements are used to model the structure (and possibly a limited bounded volume of the soil) and boundary elements are used to model the unbounded soil which is usually idealized as a horizontally stratified halfspace. The radiation conditions are implicitly satisfied if the boundary element formulation is based on the Green's functions of the stratified halfspace [14, 15].

Whereas in earthquake engineering the focus is on the low frequency range between 0 and 10 Hz, the frequency range of interest in environmental induced vibrations extends up to 80 Hz for building vibration and up to 250 Hz for re-radiated noise. The much wider frequency range of interest imposes two challenges on the computational models. The first is the greater computational cost and the second is the lack of robustness as the response prediction at high frequencies gets more sensitive to local variations of model parameters and modeling errors. The unknown or imperfectly known excitation, material and geometric properties of the model are sources of parametric uncertainty while the modeling simplifications and assumptions are sources of non-parametric uncertainty.

Although the soil is usually idealized as a horizontally stratified halfspace composed of homogeneous layers, geotechnical investigations suggest that the soil properties exhibit considerable spatial variability even within apparently homogeneous soil deposits [16]. This variability is mainly attributed to the physical processes involved in the formation of the soil layers but also to man-made activities that may perturb the properties of virgin land. Even though geotechnical and

geophysical investigations allow us to identify this variability, the spatial resolution of the information on the properties of the soil remains limited. Since the soil directly beneath a structure can have a dominant role on the structural response, the aim of this paper is to assess the influence of imperfectly known local subsoil conditions on the prediction of the response of buildings to environmental ground-borne vibration.

The dynamic SSI problem has been treated in a probabilistic setting considering parametric and non-parametric sources of uncertainty in the literature. The models focusing on parametric sources of uncertainty predate those that adopt non-parametric sources and have been mostly considering the frequency range of interest for seismic SSI problems [17, 18]. This approach requires the uncertain parameters of the model to be described by means of random variables and/or fields [19]. Subsequently, the uncertainty on the parameters of the model is propagated to the structural response with simulation methods. The models that consider non-parametric sources of uncertainty rely on the random matrix theory [20] and have been used in both seismic analyses [21] and problems of environmental vibration [22, 23]. In these models, the uncertainty is controlled by few dispersion parameters which need to be calibrated based on experimental observations.

In the present paper, the imperfectly known subsoil properties are modeled as conditional random fields following the parametric probabilistic approach formerly introduced in [24]. The parametric approach is favored over the non-parametric as it can provide insight on how the statistical and physical properties of the subsoil affect the structural response. The stochastic dynamic SSI problem is formulated based on the finite element method which provides great flexibility in incorporating any type of heterogeneity in the imperfectly known subsoil. The unbounded soil is modeled by means of perfectly matched layers [11]. An external incident wave field is incorporated in the FE-PML model by exploiting a subdomain formulation originally conceived for FE-BE formulations [13].

The remainder of this paper is organized as follows. Section 2 introduces the dynamic SSI problem and its subdomain formulation. Section 3 discusses the formulation of the dynamic SSI by means of a FE-PML model. Next, section 4 addresses the problem of statistically characterizing the uncertain local subsoil properties and the construction of the corresponding random fields. Finally, section 5 presents the results of a case study where the response of a building to ground-borne vibration is computed and the influence of the spatial correlation length of the subsoil's shear modulus and the foundation type of the building is investigated.

2. The dynamic soil-structure interaction problem

Figure 2 depicts the stochastic dynamic SSI problem where a building Ω_b is founded in a soil with imperfectly known properties. The volume of soil $\bar{\Omega}_\mathrm{s}^\mathrm{e}$ with stochastic properties is bounded and limited in the vicinity of the building while the rest of the soil $\Omega_\mathrm{s}^\mathrm{e}$ is considered deterministic. The soil-foundation interface is denoted as Σ_bs. The building is excited by an incident wave field $\hat{\mathbf{u}}_\mathrm{inc}$, where the hat above the variable denotes its representation in the frequency domain. The confinement of $\bar{\Omega}_\mathrm{s}^\mathrm{e}$ only in the vicinity of Ω_b is justified by the observation that even though the imperfectly known properties of $\Omega_\mathrm{s}^\mathrm{e}$ might influence the incident field $\hat{\mathbf{u}}_\mathrm{inc}$, they will have a rather weak impact on the dynamic stiffness of the coupled soil-structure system (section 5.4). The focus in this study is limited only to the influence of the uncertain local subsoil conditions.

The dynamic SSI problem is decomposed into two subdomains: the generalized structure $\Omega_\mathrm{r} = \Omega_\mathrm{b} \cup \bar{\Omega}_\mathrm{s}^\mathrm{e}$ and the unbounded exterior soil domain $\Omega_\mathrm{s}^\mathrm{e}$. The interface between the two subdomains is denoted as Σ_rp.

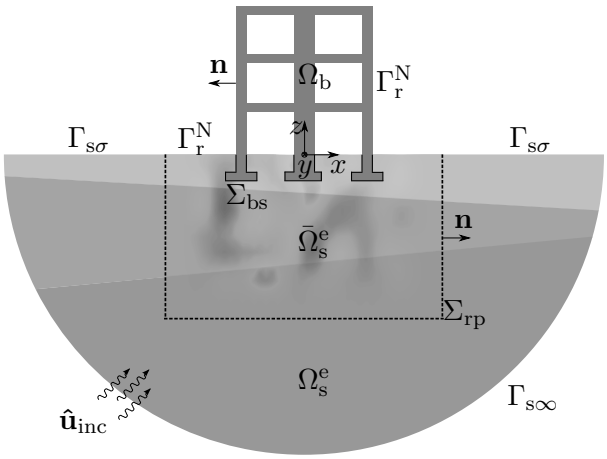

Figure 2: The stochastic dynamic SSI problem.

2.1. The generalized structure

The dynamic equilibrium equation of the generalized structure Ω_{r}, in absence of body forces, is in matrix-vector notation in the frequency domain:

$$\mathbf{L}^{\mathrm{T}}\hat{\boldsymbol{\sigma}}_{\mathrm{r}} = -\omega^2\rho_{\mathrm{r}}\hat{\mathbf{u}}_{\mathrm{r}} \qquad \text{in } \Omega_{\mathrm{r}} \tag{1}$$

where $\hat{\boldsymbol{\sigma}}_{\mathrm{r}} = \{\hat{\sigma}_{\mathrm{r}xx}, \hat{\sigma}_{\mathrm{r}yy}, \hat{\sigma}_{\mathrm{r}zz}, \hat{\sigma}_{\mathrm{r}xy}, \hat{\sigma}_{\mathrm{r}yz}, \hat{\sigma}_{\mathrm{r}zx}\}^{\mathrm{T}}$ is a vector collecting the elements of the symmetric stress tensor $\sigma_{\mathrm{r}ij}$, $\hat{\mathbf{u}}_{\mathrm{r}} = \{\hat{u}_{\mathrm{r}x}, \hat{u}_{\mathrm{r}y}, \hat{u}_{\mathrm{r}z}\}^{\mathrm{T}}$ is the displacement vector and ρ_{r} is the density. The differential operator $\mathbf{L}$ is defined as:

$$\mathbf{L} = \begin{bmatrix} \frac{\partial}{\partial x} & 0 & 0 \\ 0 & \frac{\partial}{\partial y} & 0 \\ 0 & 0 & \frac{\partial}{\partial z} \\ \frac{\partial}{\partial y} & \frac{\partial}{\partial x} & 0 \\ 0 & \frac{\partial}{\partial z} & \frac{\partial}{\partial y} \\ \frac{\partial}{\partial z} & 0 & \frac{\partial}{\partial x} \end{bmatrix} \tag{2}$$

The constitutive equation reads:

$$\hat{\boldsymbol{\sigma}}_{\mathrm{r}} = \mathbf{C}_{\mathrm{r}}\hat{\boldsymbol{\epsilon}}_{\mathrm{r}} \tag{3}$$

where the vector $\hat{\boldsymbol{\epsilon}}_{\mathrm{r}} = \{\hat{\epsilon}_{\mathrm{r}xx}, \hat{\epsilon}_{\mathrm{r}yy}, \hat{\epsilon}_{\mathrm{r}zz}, \hat{\gamma}_{\mathrm{r}xy}, \hat{\gamma}_{\mathrm{r}yz}, \hat{\gamma}_{\mathrm{r}zx}\}^{\mathrm{T}}$ collects the strains and $\mathbf{C}_{\mathrm{r}}$ is the constitutive matrix. The strain vector $\hat{\boldsymbol{\epsilon}}_{\mathrm{r}}$ is related to the displacements $\hat{\mathbf{u}}_{\mathrm{r}}$ through the kinematic equation:

$$\hat{\boldsymbol{\epsilon}}_{\mathrm{r}} = \mathbf{L}\hat{\mathbf{u}}_{\mathrm{r}} \qquad \text{in } \Omega_{\mathrm{r}} \tag{4}$$

The following Neumann boundary conditions hold on the boundary $\Gamma_{\mathrm{r}}^{\mathrm{N}}$:

$$\hat{\mathbf{t}}_{\mathrm{r}}^{\mathbf{n}}\left(\hat{\mathbf{u}}_{\mathrm{r}}\right) = \hat{\boldsymbol{\sigma}}_{\mathrm{r}} \cdot \mathbf{n} = \hat{\bar{\mathbf{t}}}_{\mathrm{r}}^{\mathbf{n}} \qquad \text{on } \Gamma_{\mathrm{r}}^{\mathrm{N}} \tag{5}$$

In addition, the following displacement continuity and traction equilibrium conditions hold on the interface Σ_{rp} :

$$\hat{\mathbf{u}}_{\mathrm{r}} = \hat{\mathbf{u}}_{\mathrm{s}} \qquad \text{on } \Sigma_{\mathrm{rp}} \tag{6}$$

$$\hat{\mathbf{t}}_{\mathrm{r}}^{\mathbf{n}}\left(\hat{\mathbf{u}}_{\mathrm{r}}\right) + \hat{\mathbf{t}}_{\mathrm{s}}^{\mathbf{n_s}}\left(\hat{\mathbf{u}}_{\mathrm{s}}\right) = \mathbf{0} \qquad \text{on } \Sigma_{\mathrm{rp}} \tag{7}$$

where $\mathbf{n_s} = -\mathbf{n}$. The virtual work equation for the generalized structure Ω_{r} is:

$$\int_{\Omega_{\mathrm{r}}} \left(\mathbf{L}\hat{\mathbf{v}}_{\mathrm{r}}\right)^{\mathrm{T}} \mathbf{C}_{\mathrm{r}} \left(\mathbf{L}\hat{\mathbf{u}}_{\mathrm{r}}\right) \,\mathrm{d}\Omega - \omega^2 \int_{\Omega_{\mathrm{r}}} \hat{\mathbf{v}}_{\mathrm{r}}^{\mathrm{T}} \rho_{\mathrm{r}} \hat{\mathbf{u}}_{\mathrm{r}} \,\mathrm{d}\Omega = \int_{\Gamma_{\mathrm{r}}^{\mathrm{N}}} \hat{\mathbf{v}}_{\mathrm{r}}^{\mathrm{T}} \hat{\doteq}^{\mathbf{n}}_{\mathrm{r}} \,\mathrm{d}\Gamma + \int_{\Sigma_{\mathrm{rp}}} \hat{\mathbf{v}}_{\mathrm{r}}^{\mathrm{T}} \hat{\mathbf{t}}_{\mathrm{r}}^{\mathbf{n}}\left(\hat{\mathbf{u}}_{\mathrm{r}}\right) \,\mathrm{d}\Gamma \tag{8}$$

where $\hat{\mathbf{v}}_{\mathrm{r}}$ is the virtual displacement field and the last integral on the right hand-side is the interaction term with the exterior soil $\Omega_{\mathrm{s}}^{\mathrm{e}}$.

2.2. The unbounded exterior soil

The dynamic equilibrium equation of the unbounded exterior soil $\Omega_{\mathrm{s}}^{\mathrm{e}}$ is in matrix-vector notation:

$$\mathbf{L}^{\mathrm{T}} \hat{\boldsymbol{\sigma}}_{\mathrm{s}} + \rho_{\mathrm{s}} \hat{\mathbf{b}}_{\mathrm{s}} = -\omega^2 \rho \hat{\mathbf{u}}_{\mathrm{s}} \qquad \text{in } \Omega_{\mathrm{s}}^{\mathrm{e}} \tag{9}$$

where $\rho_{\mathrm{s}}\hat{\mathbf{b}}_{\mathrm{s}} = \{\rho_{\mathrm{s}}\hat{\mathrm{b}}_{\mathrm{s}x}, \rho_{\mathrm{s}}\hat{\mathrm{b}}_{\mathrm{s}y}, \rho_{\mathrm{s}}\hat{\mathrm{b}}_{\mathrm{s}z}\}^{\mathrm{T}}$ is the body force vector. The following Neumann boundary conditions hold on the boundary $\Gamma_{\mathrm{s}\sigma}$:

$$\hat{\mathbf{t}}_{\mathrm{s}}^{\mathbf{n_s}}\left(\hat{\mathbf{u}}_{\mathrm{s}}\right) = \hat{\boldsymbol{\sigma}}_{\mathrm{s}} \cdot \mathbf{n_s} = \hat{\doteq}^{\mathbf{n_s}}_{\mathrm{s}} \qquad \text{on } \Gamma_{\mathrm{s}\sigma} \tag{10}$$

The body force vector $\rho_{\mathrm{s}}\hat{\mathbf{b}}_{\mathrm{s}}$ and the imposed tractions $\hat{\doteq}^{\mathbf{n_s}}_{\mathrm{s}}$ on the free surface $\Gamma_{\mathrm{s}\sigma}$ of the soil give rise to the incident wave field $\hat{\mathbf{u}}_{\mathrm{inc}}$ exciting the generalized structure Ω_{r}. The following Sommerfeld's radiation conditions, requiring the elastic waves to vanish at infinity [25], hold on the boundary $\Gamma_{\mathrm{s}\infty}$:

$$\hat{\mathbf{R}}\left(\hat{\mathbf{u}}_{\mathrm{s}}\right) = \mathbf{0} \qquad \text{on } \Gamma_{\mathrm{s}\infty} \tag{11}$$

The virtual work equation for the unbounded exterior soil $\Omega_{\mathrm{s}}^{\mathrm{e}}$ is:

$$\int_{\Omega_{\mathrm{s}}^{\mathrm{e}}} \left(\mathbf{L}\hat{\mathbf{v}}_{\mathrm{s}}\right)^{\mathrm{T}} \mathbf{C}_{\mathrm{s}} \left(\mathbf{L}\hat{\mathbf{u}}_{\mathrm{s}}\right) \,\mathrm{d}\Omega - \omega^2 \int_{\Omega_{\mathrm{s}}^{\mathrm{e}}} \hat{\mathbf{v}}_{\mathrm{s}}^{\mathrm{T}} \rho_{\mathrm{s}} \hat{\mathbf{u}}_{\mathrm{s}} \,\mathrm{d}\Omega = \int_{\Omega_{\mathrm{s}}^{\mathrm{e}}} \hat{\mathbf{v}}_{\mathrm{s}}^{\mathrm{T}} \rho_{\mathrm{s}} \hat{\mathbf{b}}_{\mathrm{s}} \,\mathrm{d}\Omega + \int_{\Gamma_{\mathrm{s}\sigma}} \hat{\mathbf{v}}_{\mathrm{s}}^{\mathrm{T}} \hat{\doteq}^{\mathbf{n_s}}_{\mathrm{s}} \,\mathrm{d}\Gamma + \int_{\Sigma_{\mathrm{rp}}} \hat{\mathbf{v}}_{\mathrm{s}}^{\mathrm{T}} \hat{\mathbf{t}}_{\mathrm{s}}^{\mathbf{n_s}}\left(\hat{\mathbf{u}}_{\mathrm{s}}\right) \,\mathrm{d}\Gamma \tag{12}$$

where $\mathbf{C}_{\mathrm{s}}$ is the constitutive matrix, ρ_{s} is the density and $\hat{\mathbf{v}}_{\mathrm{s}}$ is the virtual displacement field required to fulfill the radiation conditions (11). The last integral on the right hand-side of equation (12) is the interaction term with the generalized structure Ω_{r}.

The displacement field $\hat{\mathbf{u}}_{\mathrm{s}}$ in the unbounded exterior soil $\Omega_{\mathrm{s}}^{\mathrm{e}}$ can be decomposed into the wave field $\hat{\mathbf{u}}_0$ and the scattered wave field $\hat{\mathbf{u}}_{\mathrm{sc}}$ [13] (figure 3):

$$\hat{\mathbf{u}}_{\mathrm{s}} = \hat{\mathbf{u}}_0 + \hat{\mathbf{u}}_{\mathrm{sc}} \tag{13}$$

The wave field $\hat{\mathbf{u}}_0$ is related to the incident wave field $\hat{\mathbf{u}}_{\mathrm{inc}}$, where zero displacement boundary conditions are enforced on the interface Σ_{rp} (figure 3b), whereas the scattered wave field $\hat{\mathbf{u}}_{\mathrm{sc}}$ is

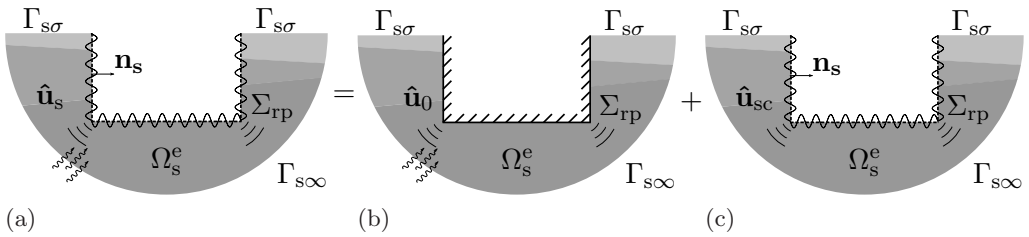

Figure 3: (a) Decomposition of the displacement field $\hat{\mathbf{u}}_s$ of the unbounded exterior soil Ω_s^e into (b) the wave field $\hat{\mathbf{u}}_0$ and (c) the diffracted displacement field $\hat{\mathbf{u}}_{sc}$.

radiated in the exterior soil Ω_s^e by the generalized structure Ω_r (figure 3c). The virtual work equation for the unbounded exterior soil Ω_s^e corresponding to the wave field $\hat{\mathbf{u}}_0$ is:

$$\int_{\Omega_s^e} (\mathbf{L}\hat{\mathbf{v}}_s)^T \mathbf{C}_s (\mathbf{L}\hat{\mathbf{u}}_0)\, d\Omega - \omega^2 \int_{\Omega_s^e} \hat{\mathbf{v}}_s^T \rho_s \hat{\mathbf{u}}_0\, d\Omega = \int_{\Omega_s^e} \hat{\mathbf{v}}_s^T \rho_s \hat{\mathbf{b}}_s\, d\Omega + \int_{\Gamma_{s\sigma}} \hat{\mathbf{v}}_s^T \hat{\mathbf{t}}_s^{\mathbf{n_s}}\, d\Gamma \tag{14}$$

where the virtual displacement field $\hat{\mathbf{v}}_s$ fulfills the radiation conditions (11) and the Dirichlet boundary conditions $\hat{\mathbf{u}}_0 = \mathbf{0}$ on the interface Σ_{rp} (figure 3b). Analogously, the virtual work equation for the unbounded exterior soil Ω_s^e corresponding to the scattered wave field $\hat{\mathbf{u}}_{sc}$ is:

$$\int_{\Omega_s^e} (\mathbf{L}\hat{\mathbf{v}}_s)^T \mathbf{C}_s (\mathbf{L}\hat{\mathbf{u}}_{sc})\, d\Omega - \omega^2 \int_{\Omega_s^e} \hat{\mathbf{v}}_s^T \rho_s \hat{\mathbf{u}}_{sc}\, d\Omega = \int_{\Sigma_{rp}} \hat{\mathbf{v}}_s^T \hat{\mathbf{t}}_s^{\mathbf{n_s}} (\hat{\mathbf{u}}_{sc})\, d\Gamma \tag{15}$$

where the virtual displacement field $\hat{\mathbf{v}}_s$ fulfills the radiation conditions (11).

2.3. The interaction problem

The dynamic SSI problem is solved enforcing the continuity of displacements and the equilibrium of tractions on the interface Σ_{rp}. Using the equilibrium condition (7), equation (8) can be written as:

$$\int_{\Omega_r} (\mathbf{L}\hat{\mathbf{v}}_r)^T \mathbf{C}_r (\mathbf{L}\hat{\mathbf{u}}_r)\, d\Omega - \omega^2 \int_{\Omega_r} \rho_r \hat{\mathbf{v}}_r^T \hat{\mathbf{u}}_r\, d\Omega = \int_{\Gamma_r^N} \hat{\mathbf{v}}_r^T \hat{\bar{\mathbf{t}}}_r^{\mathbf{n}}\, d\Gamma - \int_{\Sigma_{rp}} \hat{\mathbf{v}}_r^T \hat{\mathbf{t}}_s^{\mathbf{n_s}} (\hat{\mathbf{u}}_s)\, d\Gamma \tag{16}$$

Introducing the decomposition (13) into equation (16) and rearranging the terms yields:

$$\int_{\Omega_r} (\mathbf{L}\hat{\mathbf{v}}_r)^T \mathbf{C}_r (\mathbf{L}\hat{\mathbf{u}}_r)\, d\Omega - \omega^2 \int_{\Omega_r} \rho_r \hat{\mathbf{v}}_r^T \hat{\mathbf{u}}_r\, d\Omega + \int_{\Sigma_{rp}} \hat{\mathbf{v}}_r^T \hat{\mathbf{t}}_s^{\mathbf{n_s}} (\hat{\mathbf{u}}_{sc})\, d\Gamma = \int_{\Gamma_r^N} \hat{\mathbf{v}}_r^T \hat{\bar{\mathbf{t}}}_r^{\mathbf{n}}\, d\Gamma - \int_{\Sigma_{rp}} \hat{\mathbf{v}}_r^T \hat{\mathbf{t}}_s^{\mathbf{n_s}} (\hat{\mathbf{u}}_0)\, d\Gamma \tag{17}$$

Equation (17) can be used to solve the dynamic SSI problem by means of coupled FE-BE models. In this case, the volume integrals over Ω_r and the boundary integral on Γ_r^N are treated by means of the FE method whereas the integrals on the interface Σ_{rp} are treated by means of the BE method. Alternatively, requiring that $\hat{\mathbf{v}}_s = \hat{\mathbf{v}}_r$ on Σ_{rp} and substituting equation (15) into equation (17) allows to solve the dynamic SSI problem by means of FE in conjunction with ABC or PML:

$$\int_{\Omega_r} (\mathbf{L}\hat{\mathbf{v}}_r)^T \mathbf{C}_r (\mathbf{L}\hat{\mathbf{u}}_r)\, d\Omega - \omega^2 \int_{\Omega_r} \rho_r \hat{\mathbf{v}}_r^T \hat{\mathbf{u}}_r\, d\Omega + \int_{\Omega_s^e} (\mathbf{L}\hat{\mathbf{v}}_s)^T \mathbf{C}_s (\mathbf{L}\hat{\mathbf{u}}_{sc})\, d\Omega - \omega^2 \int_{\Omega_s^e} \rho_s \hat{\mathbf{v}}_s^T \hat{\mathbf{u}}_{sc}\, d\Omega = \int_{\Gamma_r^N} \hat{\mathbf{v}}_r^T \hat{\bar{\mathbf{t}}}_r^{\mathbf{n}}\, d\Gamma - \int_{\Sigma_{rp}} \hat{\mathbf{v}}_r^T \hat{\mathbf{t}}_s^{\mathbf{n_s}} (\hat{\mathbf{u}}_0)\, d\Gamma \tag{18}$$

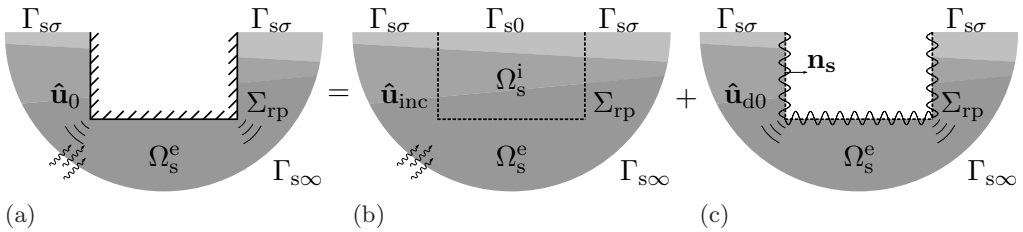

Figure 4: (a) Decomposition of the displacement field $\hat{\mathbf{u}}_0$ into (b) the incident wave field $\hat{\mathbf{u}}_{\mathrm{inc}}$ and (c) the locally diffracted displacement field $\hat{\mathbf{u}}_{\mathrm{d0}}$.

The subsequent section presents how the integrals over the unbounded volume $\Omega_{\mathrm{s}}^{\mathrm{e}}$ are replaced by integrals over the bounded volume Ω_{p} of a PML buffer zone. The integral on Σ_{rp} corresponding to the wave field $\hat{\mathbf{u}}_0$ in equations (17) and (18) is not computed directly due to the complex boundary conditions. For this reason, the wave field $\hat{\mathbf{u}}_0$ is further decomposed as [13] (figure 4):

$$\hat{\mathbf{u}}_0 = \hat{\mathbf{u}}_{\mathrm{inc}} + \hat{\mathbf{u}}_{\mathrm{d0}} \tag{19}$$

where the incident wave field $\hat{\mathbf{u}}_{\mathrm{inc}}$ and the corresponding traction field $\hat{\mathbf{t}}_{\mathrm{s}}^{\mathbf{n_s}}\left(\hat{\mathbf{u}}_{\mathrm{inc}}\right)$ are provided by a source model, generally assuming that the coupling between the subproblems of the source and the receiver can be disregarded [26] (figure 4b). In the present work, the direct stiffness method is used for this purpose [27]. The locally diffracted displacement field $\hat{\mathbf{u}}_{\mathrm{d0}}$ (figure 4c) is defined so that the combined wave field $\hat{\mathbf{u}}_{\mathrm{d0}} + \hat{\mathbf{u}}_{\mathrm{inc}}$ vanishes on Σ_{rp}. Introducing the decomposition (19) into equation (18) yields:

$$\begin{aligned}\int_{\Omega_{\mathrm{r}}} \left(\mathbf{L}\hat{\mathbf{v}}_{\mathrm{r}}\right)^{\mathrm{T}} \mathbf{C}_{\mathrm{r}} \left(\mathbf{L}\hat{\mathbf{u}}_{\mathrm{r}}\right) \,\mathrm{d}\Omega - \omega^2 \int_{\Omega_{\mathrm{r}}} \rho_{\mathrm{r}} \hat{\mathbf{v}}_{\mathrm{r}}^{\mathrm{T}} \hat{\mathbf{u}}_{\mathrm{r}} \,\mathrm{d}\Omega + \int_{\Omega_{\mathrm{s}}^{\mathrm{e}}} \left(\mathbf{L}\hat{\mathbf{v}}_{\mathrm{s}}\right)^{\mathrm{T}} \mathbf{C}_{\mathrm{s}} \left(\mathbf{L}\hat{\mathbf{u}}_{\mathrm{sc}}\right) \,\mathrm{d}\Omega - \omega^2 \int_{\Omega_{\mathrm{s}}^{\mathrm{e}}} \rho_{\mathrm{s}} \hat{\mathbf{v}}_{\mathrm{s}}^{\mathrm{T}} \hat{\mathbf{u}}_{\mathrm{sc}} \,\mathrm{d}\Omega \\ = \int_{\Gamma_{\mathrm{r}}^{\mathrm{N}}} \hat{\mathbf{v}}_{\mathrm{r}}^{\mathrm{T}} \hat{\mathbf{t}}_{\mathrm{r}}^{\hat{\mathbf{n}}} \,\mathrm{d}\Gamma - \int_{\Sigma_{\mathrm{rp}}} \hat{\mathbf{v}}_{\mathrm{r}}^{\mathrm{T}} \hat{\mathbf{t}}_{\mathrm{s}}^{\mathbf{n_s}} \left(\hat{\mathbf{u}}_{\mathrm{inc}}\right) \,\mathrm{d}\Gamma - \int_{\Sigma_{\mathrm{rp}}} \hat{\mathbf{v}}_{\mathrm{r}}^{\mathrm{T}} \hat{\mathbf{t}}_{\mathrm{s}}^{\mathbf{n_s}} \left(\hat{\mathbf{u}}_{\mathrm{d0}}\right) \,\mathrm{d}\Gamma\end{aligned} \tag{20}$$

The last integral on the right hand-side can now explicitly be computed by means of the BE method or by FE formulations in conjunction with ABC or PML as described in the following section.

3. Formulation of the FE-PML model

Figure 5a shows the stochastic dynamic SSI problem of figure 2 modeled by means of FE-PML. The computational domain consists of the generalized structure $\Omega_{\mathrm{r}} = \Omega_{\mathrm{b}} \cup \bar{\Omega}_{\mathrm{s}}^{\mathrm{e}}$ modeled with FE and the PML buffer zone Ω_{p} simulating the unbounded soil $\Omega_{\mathrm{s}}^{\mathrm{e}}$ truncated at the boundary $\Gamma_{\mathrm{p}}^{\mathrm{D}}$. The material properties of $\bar{\Omega}_{\mathrm{s}}^{\mathrm{e}}$ are modeled as conditional random fields (section 4.2) with a small zone of soil close to Σ_{rp} having deterministic properties. The FE-PML model is developed based on the 3D elastodynamic equations in the frequency domain.

3.1. The PML buffer zone

To absorb waves inside the PML buffer zone Ω_{p} the dynamic equilibrium equation and kinematic equation are modified by introducing complex coordinate stretching (figure 6) [10, 28]. For a coordinate s, representing the x, y or z coordinate, the stretched coordinate $\tilde{s}$ is defined as:

$$\tilde{s} = s_{\mathrm{o}} + \int_{s_{\mathrm{o}}}^{s_{\mathrm{t}}} \hat{\lambda}_{\mathrm{s}}(s) \,\mathrm{d}s \tag{21}$$

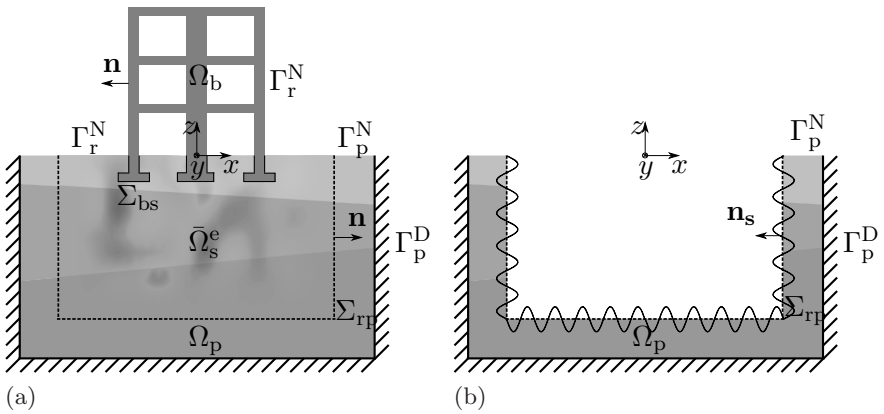

Figure 5: (a) FE-PML model of the stochastic dynamic SSI problem of figure 2 and (b) FE-PML model of the truncated unbounded soil.

where s_o and s_t delimit the origin and the termination of the PML buffer zone in the direction of the coordinate s, and $\hat{\lambda}_s(s)$ is the considered stretch function:

$$\hat{\lambda}_s(s) = \alpha_{0s}(s) + \frac{\alpha_{1s}(s)}{i\omega} \tag{22}$$

with $\alpha_{0s}(s)$ and $\alpha_{1s}(s)$ polynomial functions that control the attenuation of the evanescent and propagating waves inside the PML buffer zone [29]. In the present work, they are defined as:

$$\alpha_{0s}(s) = \begin{cases} 1 + \alpha_0 \left(\dfrac{|s - s_o|}{L_s} \right)^q & s_o \leq s \leq s_t \\ 1 & s < s_o \end{cases} \tag{23}$$

$$\alpha_{1s}(s) = \begin{cases} \alpha_1 \left(\dfrac{|s - s_o|}{L_s} \right)^q & s_o \leq s \leq s_t \\ 0 & s < s_o \end{cases} \tag{24}$$

where L_s is the thickness of the PML buffer zone in the direction of the coordinate s, α_0 and α_1 are tuning parameters, and $q = 3$ is the degree of the polynomial attenuation. Starting from equation (21), the partial derivative with respect to $\tilde{s}$ is written as:

$$\frac{\partial}{\partial \tilde{s}} = \frac{1}{\hat{\lambda}_s(s)} \frac{\partial}{\partial s} \tag{25}$$

The modified dynamic equilibrium for the PML buffer zone Ω_p is obtained by introducing the stretched coordinates according to the transformation defined by equation (25) into equation (9):

$$\hat{\lambda}_x \hat{\lambda}_y \hat{\lambda}_z \tilde{\mathbf{L}}^T \hat{\boldsymbol{\sigma}}_p = -\omega^2 \rho_p \hat{\lambda}_x \hat{\lambda}_y \hat{\lambda}_z \hat{\mathbf{u}}_p \qquad \text{in } \Omega_p \tag{26}$$

Similarly, the modified kinematic equation is:

$$\hat{\boldsymbol{\epsilon}}_p = \tilde{\mathbf{L}} \hat{\mathbf{u}}_p \qquad \text{in } \Omega_p \tag{27}$$

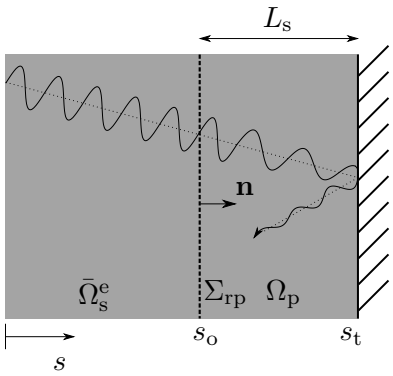

Figure 6: PML in the direction of coordinate s. The waves enter into the PML buffer zone without any spurious reflections at the interface Σ_{rp} and gradually decay within the PML.

where the equilibrium equation (26) has also been multiplied by a factor $\hat{\lambda}_x\hat{\lambda}_y\hat{\lambda}_z$ and the modified differential operator $\tilde{\mathbf{L}}$ is defined as:

$$\tilde{\mathbf{L}} = \begin{bmatrix} \frac{1}{\hat{\lambda}_x}\frac{\partial}{\partial x} & 0 & 0 \\ 0 & \frac{1}{\hat{\lambda}_y}\frac{\partial}{\partial y} & 0 \\ 0 & 0 & \frac{1}{\hat{\lambda}_z}\frac{\partial}{\partial z} \\ \frac{1}{\hat{\lambda}_y}\frac{\partial}{\partial y} & \frac{1}{\hat{\lambda}_x}\frac{\partial}{\partial x} & 0 \\ 0 & \frac{1}{\hat{\lambda}_z}\frac{\partial}{\partial z} & \frac{1}{\hat{\lambda}_y}\frac{\partial}{\partial y} \\ \frac{1}{\hat{\lambda}_z}\frac{\partial}{\partial z} & 0 & \frac{1}{\hat{\lambda}_x}\frac{\partial}{\partial x} \end{bmatrix} \tag{28}$$

The following Neumann and Dirichlet boundary conditions apply on the boundaries $\Gamma_{\mathrm{p}}^{\mathrm{N}}$ and $\Gamma_{\mathrm{p}}^{\mathrm{D}}$ of the PML buffer zone (figure 5a):

$$\hat{\mathbf{t}}_{\mathrm{p}}^{\mathbf{n_s}}\left(\hat{\mathbf{u}}_{\mathrm{p}}\right) = \hat{\boldsymbol{\sigma}}_{\mathrm{p}} \cdot \mathbf{n} = \mathbf{0} \qquad \text{on } \Gamma_{\mathrm{p}}^{\mathrm{N}} \tag{29}$$

$$\hat{\mathbf{u}}_{\mathrm{p}} = \mathbf{0} \qquad \text{on } \Gamma_{\mathrm{p}}^{\mathrm{D}} \tag{30}$$

The virtual work expression of the dynamic SSI model depicted in figure 5a is obtained by replacing the integrals over $\Omega_{\mathrm{s}}^{\mathrm{e}}$ in equation (20) with integrals over the PML buffer zone Ω_{p}:

$$\begin{aligned} &\int_{\Omega_{\mathrm{r}}} \left(\mathbf{L}\hat{\mathbf{v}}_{\mathrm{r}}\right)^{\mathrm{T}} \mathbf{C}_{\mathrm{r}} \left(\mathbf{L}\hat{\mathbf{u}}_{\mathrm{r}}\right) \mathrm{d}\Omega - \omega^2 \int_{\Omega_{\mathrm{r}}} \rho_{\mathrm{r}} \hat{\mathbf{v}}_{\mathrm{r}}^{\mathrm{T}} \hat{\mathbf{u}}_{\mathrm{r}} \, \mathrm{d}\Omega + \int_{\Omega_{\mathrm{p}}} \hat{\lambda}_x\hat{\lambda}_y\hat{\lambda}_z \left(\tilde{\mathbf{L}}\hat{\mathbf{v}}_{\mathrm{p}}\right)^{\mathrm{T}} \mathbf{C}_{\mathrm{p}} \left(\tilde{\mathbf{L}}\hat{\mathbf{u}}_{\mathrm{p}}\right) \mathrm{d}\Omega \\ &-\omega^2 \int_{\Omega_{\mathrm{p}}} \rho_{\mathrm{p}} \hat{\lambda}_x\hat{\lambda}_y\hat{\lambda}_z \hat{\mathbf{v}}_{\mathrm{p}}^{\mathrm{T}} \hat{\mathbf{u}}_{\mathrm{p}} \, \mathrm{d}\Omega = \int_{\Gamma_{\mathrm{r}}^{\mathrm{N}}} \hat{\mathbf{v}}_{\mathrm{r}}^{\mathrm{T}} \hat{\mathbf{t}}_{\mathrm{r}}^{\hat{\mathbf{n}}} \, \mathrm{d}\Gamma - \int_{\Sigma_{\mathrm{rp}}} \hat{\mathbf{v}}_{\mathrm{r}}^{\mathrm{T}} \hat{\mathbf{t}}_{\mathrm{s}}^{\mathbf{n_s}} \left(\hat{\mathbf{u}}_{\mathrm{inc}}\right) \mathrm{d}\Gamma - \int_{\Sigma_{\mathrm{rp}}} \hat{\mathbf{v}}_{\mathrm{r}}^{\mathrm{T}} \hat{\mathbf{t}}_{\mathrm{s}}^{\mathbf{n_s}} \left(\hat{\mathbf{u}}_{\mathrm{d0}}\right) \mathrm{d}\Gamma \end{aligned} \tag{31}$$

where now the virtual displacement field $\hat{\mathbf{v}}_{\mathrm{p}}$ is required to fulfill the Dirichlet boundary conditions on $\Gamma_{\mathrm{p}}^{\mathrm{D}}$.

3.2. FE discretization

Subsequently, a standard Galerkin procedure is followed, where the same shape functions are used to approximate both the displacement fields $\hat{\mathbf{u}} = \{\hat{\mathbf{u}}_{\mathrm{r}}, \hat{\mathbf{u}}_{\mathrm{p}}\}^{\mathrm{T}}$ and $\hat{\mathbf{v}} = \{\hat{\mathbf{v}}_{\mathrm{r}}, \hat{\mathbf{v}}_{\mathrm{p}}\}^{\mathrm{T}}$:

$$\hat{\mathbf{u}} \simeq \mathbf{N}\underline{\hat{\mathbf{u}}} \quad \text{and} \quad \hat{\mathbf{v}} \simeq \mathbf{N}\underline{\hat{\mathbf{v}}} \tag{32}$$

where $\mathbf{N} \in \mathbb{R}^{3\times n}$ is a matrix containing the globally defined shape functions with n the number of degrees of freedom in the model and the vector $\underline{\hat{\mathbf{u}}} = \{\underline{\hat{\mathbf{u}}}_\mathrm{r}, \underline{\hat{\mathbf{u}}}_\mathrm{p}\}^\mathrm{T} \in \mathbb{C}^n$ collects the nodal displacements of the FE-PML model. Since equation (31) holds for any virtual displacement field $\hat{\mathbf{v}}$ fulfilling the Dirichlet boundary conditions on $\Gamma_\mathrm{p}^\mathrm{D}$, the following system of equations is obtained by introducing the approximations (32) into equation (31):

$$\left(\int_{\Omega_\mathrm{r}} \mathbf{B}^\mathrm{T}\mathbf{C}_\mathrm{r}\mathbf{B}\,\mathrm{d}\Omega - \omega^2\int_{\Omega_\mathrm{r}} \rho_\mathrm{r}\mathbf{N}^\mathrm{T}\mathbf{N}\,\mathrm{d}\Omega + \int_{\Omega_\mathrm{p}} \hat{\lambda}_x\hat{\lambda}_y\hat{\lambda}_z\tilde{\mathbf{B}}^\mathrm{T}\mathbf{C}_\mathrm{s}\tilde{\mathbf{B}}\,\mathrm{d}\Omega - \omega^2\int_{\Omega_\mathrm{p}} \rho_\mathrm{s}\hat{\lambda}_x\hat{\lambda}_y\hat{\lambda}_z\mathbf{N}^\mathrm{T}\mathbf{N}\,\mathrm{d}\Omega\right)\underline{\hat{\mathbf{u}}} = \int_{\Gamma_\mathrm{r}^\mathrm{N}} \mathbf{N}^\mathrm{T}\hat{\mathbf{t}}_\mathrm{r}^{\hat{\mathbf{n}}}\,\mathrm{d}\Gamma - \int_{\Sigma_\mathrm{rp}} \mathbf{N}^\mathrm{T}\hat{\mathbf{t}}_\mathrm{s}^{\mathbf{n_s}}\left(\hat{\mathbf{u}}_\mathrm{inc}\right)\,\mathrm{d}\Gamma - \int_{\Sigma_\mathrm{rp}} \mathbf{N}^\mathrm{T}\hat{\mathbf{t}}_\mathrm{s}^{\mathbf{n_s}}\left(\hat{\mathbf{u}}_\mathrm{d0}\right)\,\mathrm{d}\Gamma \tag{33}$$

where $\mathbf{B} = \mathbf{L}\mathbf{N} \in \mathbb{R}^{6\times n}$ and $\tilde{\mathbf{B}} = \tilde{\mathbf{L}}\mathbf{N} \in \mathbb{C}^{6\times n}$ are matrices containing the derivatives of the globally defined shape functions. The system of equations (33) can be written in compact form as:

$$\hat{\mathbf{S}}\underline{\hat{\mathbf{u}}} = \underline{\hat{\mathbf{f}}} \tag{34}$$

where $\hat{\mathbf{S}} \in \mathbb{C}^{n\times n}$ is the dynamic stiffness matrix of the system and $\underline{\hat{\mathbf{f}}} \in \mathbb{C}^n$ is the vector collecting the nodal loads. Since the material properties in part of $\bar{\Omega}_\mathrm{s}^\mathrm{e}$ are modeled as conditional random fields, some elements of the dynamic stiffness matrix $\hat{\mathbf{S}}$ are stochastic. The mapping of the stochastic material properties of $\bar{\Omega}_\mathrm{s}^\mathrm{e}$ onto the FE mesh is addressed in section 4.3.

Following the definition of the locally diffracted displacement field $\hat{\mathbf{u}}_\mathrm{d0}$, the last integral on the right-hand side of equation (33) is implicitly evaluated by computing directly the reaction forces $\underline{\hat{\mathbf{f}}}_\mathrm{d0}$ on the interface Σ_rp of the FE-PML model (figure 5b) due to imposed displacements $\underline{\hat{\mathbf{u}}}_\mathrm{d0} = -\underline{\hat{\mathbf{u}}}_\mathrm{inc}$ on Σ_rp:

$$\int_{\Sigma_\mathrm{rp}} \mathbf{N}^\mathrm{T}\hat{\mathbf{t}}^{\mathbf{n_s}}\left(\hat{\mathbf{u}}_\mathrm{d0}\right)\,\mathrm{d}\Gamma = \left\{\begin{array}{c}\mathbf{0}\\ \underline{\hat{\mathbf{f}}}_\mathrm{d0}\\ \mathbf{0}\end{array}\right\} \tag{35}$$

The system of equations of the FE-PML model is in this case:

$$\left[\begin{array}{cc}\hat{\mathbf{S}}_\mathrm{oo} & \hat{\mathbf{S}}_\mathrm{ot}\\ \hat{\mathbf{S}}_\mathrm{to} & \hat{\mathbf{S}}_\mathrm{tt}\end{array}\right]\left\{\begin{array}{c}-\underline{\hat{\mathbf{u}}}_\mathrm{inc}\\ \underline{\hat{\mathbf{u}}}_\mathrm{t}\end{array}\right\} = \left\{\begin{array}{c}\underline{\hat{\mathbf{f}}}_\mathrm{d0}\\ \mathbf{0}\end{array}\right\} \tag{36}$$

where the subscript o denotes the degrees of freedom on the interface Σ_rp whereas the subscript t denotes the internal degrees of freedom of the PML buffer zone Ω_p. Rearranging and solving the system of equations (36) with respect to $\underline{\hat{\mathbf{f}}}_\mathrm{d0}$ yields:

$$\underline{\hat{\mathbf{f}}}_\mathrm{d0} = -\left(\hat{\mathbf{S}}_\mathrm{oo} - \hat{\mathbf{S}}_\mathrm{ot}\hat{\mathbf{S}}_\mathrm{tt}^{-1}\hat{\mathbf{S}}_\mathrm{to}\right)\underline{\hat{\mathbf{u}}}_\mathrm{inc} \tag{37}$$

4. Local subsoil conditions

The subsoil in $\bar{\Omega}_\mathrm{s}^\mathrm{e}$ is modeled as a heterogeneous isotropic elastic medium with imperfectly known elastic properties. A problem of parametric uncertainty is considered where the elastic properties are represented by random fields. In order to construct these fields, sufficient information on the statistical characteristics of the elastic parameters is required. Section 4.1 discusses the parameterization of the subsoil properties. Subsequently, the corresponding random fields and their mapping onto the finite element mesh are addressed in section 4.2 and 4.3.

4.1. Statistical characterization of subsoil conditions

The bulk modulus K and the shear modulus G of the soil, as multiples of the eigenvalues of the constitutive matrix $\mathbf{C}$, are strictly positive without any other physical constraint. This makes them appealing parameters to statistically characterize the elastic properties of the soil [30]. Statistically, the bulk modulus K and the shear modulus G are strongly correlated with the ratio K/G depending on the Poisson's ratio ν:

$$\frac{K}{G} = \frac{2\left(1+\nu\right)}{3\left(1-2\nu\right)} \tag{38}$$

of which the variation is rather limited within apparently homogeneous deposits [31]. Although laboratory and in situ tests allow to determine the bulk modulus K and the shear modulus G, it is practically unfeasible to measure their continuous spatial variation in detail. In situ tests involve averaging of the moduli values over a considerable volume of soil while laboratory tests provide estimations at discrete locations. Geotechnical tests like the cone penetration test (CPT) allow to measure soil strength parameters at a fine spatial resolution. Empirical data suggest that the strength and elastic parameters of certain soil types are strongly correlated [32] and it can therefore be assumed that they vary spatially in a similar way. In this case, the spatial correlation length l_c of the shear modulus G can be implicitly elicited from that of CPT data. Depending on the soil type, the spatial correlation length of typical CPT data ranges from few centimeters to few meters for the micro-scale soil variability [33].

The probability density function (PDF) of the shear modulus G is constructed based on the maximum entropy principle which yields the Gamma distribution as the one that maximizes the uncertainty under the conditions that the shear modulus has a strictly positive support with prescribed mean and the response of the stochastic system attains finite variance [34, 35]. As the variation of the Poisson's ratio ν and the material density ρ of the soil is generally limited [16], both are considered deterministic in the following.

4.2. Random field modeling

The shear modulus G of the soil in $\bar{\Omega}_\mathrm{s}^\mathrm{e}$ is modeled as a random field $G(\mathbf{x},\theta)$ defined over the space $\mathbf{x} \in \bar{\Omega}_\mathrm{s}^\mathrm{e}$ [19]. The probabilistic characterization of the stochastic shear modulus $G(\mathbf{x},\theta)$ is based on its marginal probability distribution function (PDF) $p_\mathrm{G}\left(\theta\right)$, mean $\mu_\mathrm{G}\left(\mathbf{x}\right)$, variance $\sigma_\mathrm{G}^2\left(\mathbf{x}\right)$ and auto-correlation coefficient $\rho_\mathrm{GG}\left(\mathbf{x},\mathbf{x'}\right)$ functions. The covariance function $C_\mathrm{GG}\left(\mathbf{x},\mathbf{x'}\right)$ is then defined as:

$$C_\mathrm{GG}\left(\mathbf{x},\mathbf{x'}\right) = \sigma_\mathrm{G}\left(\mathbf{x}\right)\sigma_\mathrm{G}\left(\mathbf{x'}\right)\rho_\mathrm{GG}\left(\mathbf{x},\mathbf{x'}\right) \tag{39}$$

A computationally tractable approximation of the stochastic shear modulus $G(\mathbf{x},\theta)$ is obtained by reducing its representation into a finite set of random variables. In this work, this is achieved by discretizing the continuous space $\mathbf{x} \in \bar{\Omega}_\mathrm{s}^\mathrm{e}$ into a finite set of control points $\mathbf{x}_k \in \bar{\Omega}_\mathrm{s}^\mathrm{e}$, $k \in \{1,...,n_k\}$ where the distance between the control points $\mathbf{x}_k$ is dictated by its covariance function $C_\mathrm{GG}\left(\mathbf{x},\mathbf{x'}\right)$ [36]. After discretization, the random field $G(\mathbf{x},\theta)$ is reduced to a random vector $\mathbf{G}\left(\theta\right)$ corresponding to the values of the random field at the control points $\mathbf{x}_k \in \bar{\Omega}_\mathrm{s}^\mathrm{e}$.

The stochastic shear modulus $\mathbf{G}\left(\theta\right)$ is simulated through a translation process based on the Nataf multivariate distribution [37]. This defines the non-Gaussian shear modulus $\mathbf{G}\left(\theta\right)$ as a non-linear transformation of a Gaussian random vector $\boldsymbol{\mathcal{G}}\left(\theta\right)$. For the k-th element $G_k\left(\theta\right)$ of $\mathbf{G}\left(\theta\right)$ this

transformation is:

$$G_k(\theta) = P_\Gamma^{-1}\left(P_{\mathrm{N}}\left(\frac{\mathcal{G}_k(\theta) - \mu_{\mathcal{G}k}}{\sigma_{\mathcal{G}k}}\right)\right) \tag{40}$$

where P_Γ^{-1} is the inverse of the target Gamma marginal cumulative distribution function (CDF), P_{N} is the standard normal CDF function, and $\boldsymbol{\mu}_{\mathcal{G}} = \boldsymbol{\mu}_{\mathrm{G}}$ and $\boldsymbol{\sigma}_{\mathcal{G}} = \boldsymbol{\sigma}_{\mathrm{G}}$ are the mean and variance of $\boldsymbol{\mathcal{G}}(\theta)$. Based on this translation process, the correlation coefficient matrix $\boldsymbol{\rho}_{\mathcal{G}\mathcal{G}}$ of the underlying Gaussian vector is computed by means of an iterative scheme in order to obtain a random vector with the target correlation coefficient matrix $\boldsymbol{\rho}_{\mathrm{GG}}$ [37].

In order for the realizations of the shear modulus of the soil to be continuous at the interface Σ_{rp} between $\bar{\Omega}_{\mathrm{s}}^{\mathrm{e}}$ and $\Omega_{\mathrm{s}}^{\mathrm{e}}$, the shear modulus $\boldsymbol{\mathcal{G}}(\theta)$ is modeled as a conditional random vector $\bar{\boldsymbol{\mathcal{G}}}(\theta)$ with prescribed deterministic values on Σ_{rp}. The conditional distribution of a Gaussian random vector $\boldsymbol{\mathcal{G}}(\theta)$, given known values $\mathcal{G}_l(\theta) = \bar{\mathcal{G}}_l$ at $\mathbf{x}_l \in \Sigma_{\mathrm{rp}}$, $l \in \{1, ..., n_l\}$, is also Gaussian with modified mean and covariance [19]:

$$\bar{\boldsymbol{\mu}}_{\mathcal{G}} = \boldsymbol{\mu}_{\mathcal{G}} + \mathbf{C}_{\bar{\mathcal{G}}\mathcal{G}}^{\mathrm{T}} \mathbf{C}_{\bar{\mathcal{G}}\bar{\mathcal{G}}}^{-1} \boldsymbol{\Delta}\bar{\boldsymbol{\mathcal{G}}} \tag{41}$$

$$\bar{\mathbf{C}}_{\mathcal{G}\mathcal{G}} = \mathbf{C}_{\mathcal{G}\mathcal{G}} - \mathbf{C}_{\bar{\mathcal{G}}\mathcal{G}}^{\mathrm{T}} \mathbf{C}_{\bar{\mathcal{G}}\bar{\mathcal{G}}}^{-1} \mathbf{C}_{\bar{\mathcal{G}}\mathcal{G}} \tag{42}$$

where the vector $\boldsymbol{\Delta}\bar{\boldsymbol{\mathcal{G}}}$ is defined as:

$$\boldsymbol{\Delta}\bar{\boldsymbol{\mathcal{G}}} = \{\bar{\mathcal{G}}_1 - \mu_{\mathcal{G}1}, ..., \bar{\mathcal{G}}_{\mathrm{n_l}} - \mu_{\mathcal{G}\mathrm{n_l}}\}^{\mathrm{T}} \tag{43}$$

with $\mathbf{C}_{\bar{\mathcal{G}}\mathcal{G}}$ the cross-covariance between $\boldsymbol{\mathcal{G}}(\theta)$ and $\mathcal{G}_l(\theta) = \bar{\mathcal{G}}_l$ and $\mathbf{C}_{\bar{\mathcal{G}}\bar{\mathcal{G}}}$ the covariance matrix of $\mathcal{G}_l(\theta) = \bar{\mathcal{G}}_l$. Realizations of the random vector $\bar{\boldsymbol{\mathcal{G}}}(\theta)$ are then generated as:

$$\bar{\boldsymbol{\mathcal{G}}}(\theta) \approx \bar{\boldsymbol{\mu}}_{\mathcal{G}} + \sum_{k=1}^{n_m} \xi_k(\theta) \sqrt{\lambda_k} \boldsymbol{\phi}_k \tag{44}$$

where λ_k and $\boldsymbol{\phi}_k$ are the k-th eigenvalue and eigenvector of the covariance matrix $\bar{\mathbf{C}}_{\mathcal{G}\mathcal{G}}$ and $\xi_k(\theta)$ are random variables sampled from the standard Gaussian distribution $\mathcal{N}(0,1)$. In order to improve the representativeness of the sampled pool of realizations, Latin hypercube sampling with artificial correlation reduction is used [38]. This sampling scheme explores the event space Θ more uniformly avoiding the formation of clusters of realizations that might stall convergence. The number $n_m \leq n_k$ of eigenpairs $(\lambda_k, \boldsymbol{\phi}_k)$ included in the expansion (44) can be decided based on a maximum acceptable relative truncation error:

$$\epsilon(n_m) = 1 - \frac{1}{\mathrm{Tr}\left(\bar{\mathbf{C}}_{\mathcal{G}\mathcal{G}}\right)} \sum_{k=1}^{n_m} \lambda_k \leq \epsilon_{\max} \tag{45}$$

where $\mathrm{Tr}(\cdot)$ denotes the trace of a matrix.

4.3. Mapping of the stochastic subsoil properties onto the FE mesh

The realizations of the random vector $\bar{\boldsymbol{\mathcal{G}}}(\theta)$ are used as input for the expansion optimal linear estimation (EOLE) method to interpolate the random field $\bar{\mathcal{G}}(\mathbf{x}, \theta)$ at any point $\mathbf{x} \in \bar{\Omega}_{\mathrm{s}}^{\mathrm{e}}$ [36]:

$$\bar{\mathcal{G}}(\mathbf{x}, \theta) \approx \bar{\mu}_{\mathcal{G}}(\mathbf{x}) + \bar{\mathbf{C}}_{\mathcal{G}\bar{\mathcal{G}}}^{\mathrm{T}}(\mathbf{x}) \bar{\mathbf{C}}_{\mathcal{G}\mathcal{G}}^{-1} \sum_{k=1}^{n_m} \xi_k(\theta) \sqrt{\lambda_k} \boldsymbol{\phi}_k \tag{46}$$

where $\bar{\mathbf{C}}_{\mathcal{G}\bar{\mathcal{G}}}(\mathbf{x})$ is the cross-covariance vector function between $\bar{\boldsymbol{\mathcal{G}}}(\theta)$ and $\bar{\mathcal{G}}(\mathbf{x},\theta)$. Subsequently, application of the non-linear transformation defined by equation (40) provides the desired non-Gaussian realizations $\bar{G}(\mathbf{x},\theta)$.

The dynamic stiffness matrix $\hat{\mathbf{S}}$ in equation (34) is formulated taking into account the continuous variation of the shear modulus $\bar{G}(\mathbf{x},\theta)$ in $\bar{\Omega}_{\mathrm{s}}^{\mathrm{e}}$. As the random field discretization and the finite element discretization are not necessarily coinciding, the stochastic shear modulus is first evaluated at the finite element nodes of $\bar{\Omega}_{\mathrm{s}}^{\mathrm{e}}$ by means of equation (46) for each realization and subsequently interpolated at the FE integration points using the displacement interpolation functions (32) [39]. In order to accurately resolve the spatial fluctuations of the shear modulus, this approach requires the finite element mesh to be at least as fine as the random field discretization.

5. Case study

5.1. Model description

The influence of imperfectly known local subsoil conditions on the response of buildings to ground-borne environmental vibrations is assessed in a case study. A three storey reinforced concrete office building is considered. Figure 7 shows the floor layout of the building and table 1 summarizes its characteristics where h_{s} is the storey height and t_{s} the slab thickness. Two different cases are examined for the building's foundation: a) a raft foundation with thickness $t_{\mathrm{f}} = 0.60$ m, and b) individual footings with thickness $t_{\mathrm{f}} = 0.40$ m for the base of each column and wall. The mean dynamic characteristics of the halfspace representing the soil underneath the building are summarized in table 2 where C_{s} denotes the shear wave velocity, C_{p} the dilatational wave velocity, and β_{s} and β_{p} represent the hysteretic material damping ratio for the shear waves and the dilatational waves, respectively. The frequency independent hysteretic material damping in the soil is introduced using complex Lamé coefficients $\mu(1+2\beta_{\mathrm{s}}i)$ and $(\lambda+2\mu)(1+2\beta_{\mathrm{p}}i)$ according to the correspondence principle [40, 41]. The building response is investigated by computing transfer functions which relate the building displacements to a unit vertical force (1 N/Hz) that is applied at the surface of the halfspace at the point $S(-34\,\mathrm{m}, -26\,\mathrm{m}, 0\,\mathrm{m})$ with respect to the origin of the reference system. The analysis is performed in the frequency range between 1 Hz and 80 Hz which is of interest for problems of environmental ground vibration.

Table 1: Building characteristics (figure 7).

h_{s} [m]	t_{s} [m]	C [m × m]	B [m × m]	W_x [m × m]	W_y [m × m]	E_{s} [GPa]	ρ_{s} [kg/m^3]
3	0.15	0.35 × 0.35	0.20 × 0.50	1.50 × 0.20	0.20 × 1.50	30	2500

Table 2: Mean dynamic soil characteristics.

h [m]	C_{s} [m/s]	C_{p} [m/s]	G [MPa]	ν [−]	ρ [kg/m^3]	$\beta_{\mathrm{s}} = \beta_{\mathrm{p}}$ [−]
∞	300	600	162	1/3	1800	0.01

Figure 8 shows the FE-PML model. The subsoil is discretized with 3D twenty-node finite elements. A maximum element size $l_{\mathrm{e}} = 0.75$ m is used for the mesh, corresponding to 5 quadratic

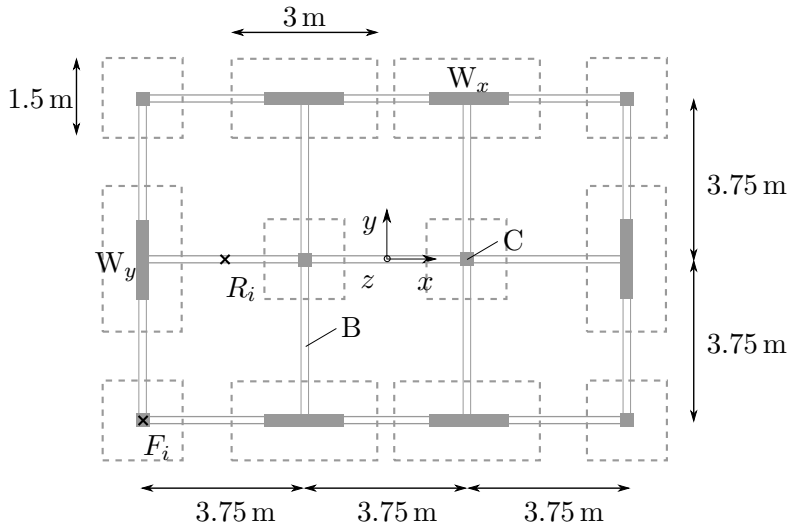

Figure 7: Building layout at the i-th floor ($i = 0, 1, 2, 3$) where W_x and W_y denote the walls in the x- and the y-direction, C the columns and B the beams. The outline of the foundation footings is shown with dashed lines. The receiver locations R_i and F_i at the i-th floor are indicated with $\times$. The receiver locations F_0, R_1 and R_3 considered next are located on the foundation level, the first floor and the roof of the building, respectively.

finite elements per shear wavelength λ_s at a frequency of 80 Hz. The building is modeled with frame and eight-node shell elements; hysteretic damping is assumed with $\eta = 0.05$ [42].

The effectiveness of the PML strongly depends on the stretch function parameters and the finite element mesh. For computational efficiency, two meshes are used for the PML, (a) a mesh with $L_\mathrm{s} = 2.25$ m for the frequency range between 1 Hz and 10 Hz and (b) a mesh with $L_\mathrm{s} = 1.50$ m for the frequency range between 10 Hz and 80 Hz. Because the real part $\alpha_{0\mathrm{s}}(s)$ of the stretch functions modifies the wavelength $\tilde{\lambda} = \lambda/(1 + \alpha_{0\mathrm{s}}(s))$ inside the PML [43], $\alpha_0(\omega)$ is defined at each frequency ω so that at least two quadratic finite elements per shear wavelength are present inside the PML buffer zone:

$$\alpha_0(\omega) = \frac{\pi}{l_\mathrm{e}} \frac{C_\mathrm{s}}{\omega} - 1 \tag{47}$$

The value of $\alpha_1(\omega)$ is defined based on recommended values in the literature [11]:

$$\alpha_1(\omega) = 20 \frac{C_\mathrm{s}}{\omega} \tag{48}$$

The shear modulus of the soil in $\bar{\Omega}_\mathrm{s}^\mathrm{e}$ (figure 8) is modeled as a conditional random field $\bar{G}(\mathbf{x}, \theta)$ with a Gamma marginal PDF and a coefficient of variation $\mathrm{CoV} = 0.25$ according to the methodology outlined in section 4.2 (figure 9a). An isotropic squared exponential correlation coefficient function is assumed for the covariance of the unconditional random field $G(\mathbf{x}, \theta)$ which ensures continuous field realizations [36]:

$$C_\mathrm{GG}(\mathbf{x}, \mathbf{x'}) = \sigma_\mathrm{G}^2 \exp\left(-\frac{|\mathbf{x} - \mathbf{x'}|^2}{l_\mathrm{c}^2}\right) \tag{49}$$

The variation of the material properties in soil deposits is generally anisotropic with different correlation lengths in the vertical and horizontal directions [33]. Nevertheless, a single isotropic

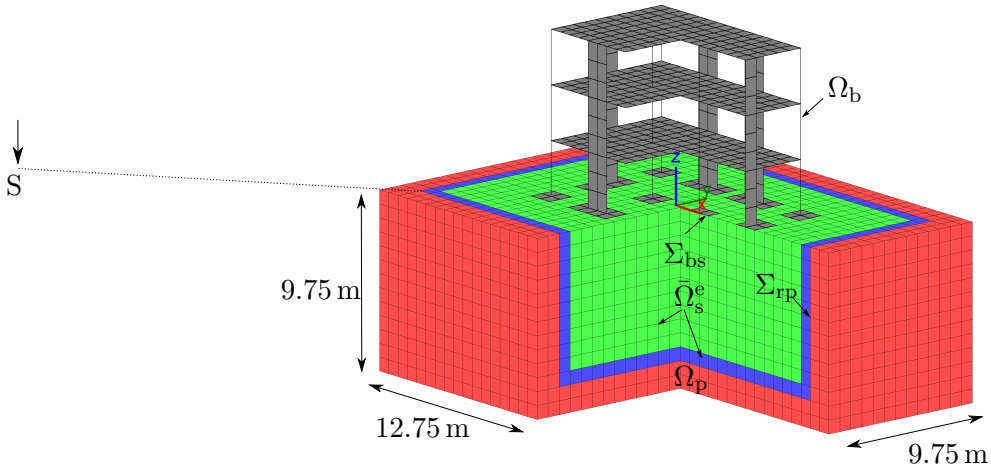

Figure 8: FE-PML model for the frequency range between 10 Hz and 80 Hz in the case of the building with individual footings. The model subdomains are in accordance with figure 5a.

correlation length l_c is considered in the present study which allows to develop a general understanding of how the variability of the local subsoil properties affects the structural response. Two correlation lengths are examined: (a) $l_c = 1$ m and (b) $l_c = 1.50$ m.In both cases, the discretization length of the random field is $3l_c/4$.

The realizations of the stochastic shear modulus are generated for a relative truncation error $\epsilon_{max} = 0.05$ according to equation (45) (figure 9b). This corresponds to $n_m = 994$ random variables in the case with $l_c = 1$ m and $n_m = 720$ random variables in the case with $l_c = 1.50$ m. Figures 10b and 10c show two realizations of the stochastic shear modulus of the soil mapped onto the finite element mesh for the two correlation lengths considered. The realizations of the shear modulus are constrained to take the deterministic value of the exterior soil Ω_s^e on the interface Σ_{rp}.

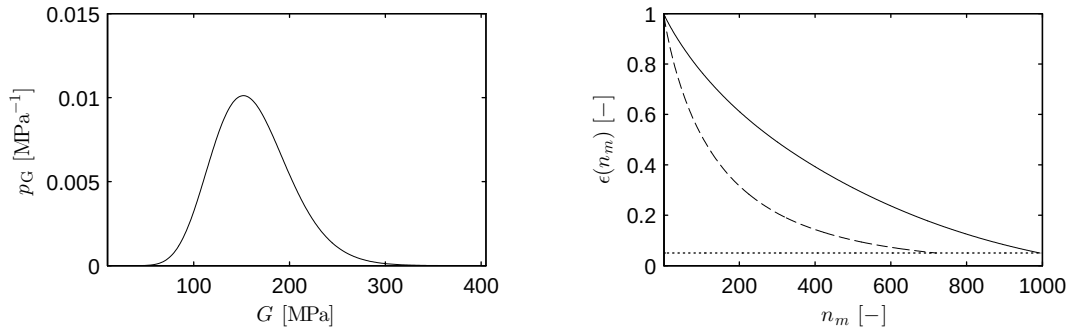

(a) (b)

Figure 9: (a) Gamma marginal PDF of the stochastic shear modulus, and (b) relative truncation error $\epsilon(n_m)$ for $l_c = 1$ m (solid line), $l_c = 1.50$ m (dashed line) and $\epsilon_{max} = 0.05$ (dotted line).

5.2. Model verification

Before proceeding to the case study with uncertain local subsoil conditions, the FE-PML model is verified. To this end, the Green's functions of the homogeneous halfspace with the properties of table 2 are computed without the presence of the building (figure 10a). Figure 11 compares the transfer functions of the vertical displacement along the x-axis computed with the FE-PML model and the direct stiffness method [27]. The transfer functions computed with the two models are in good agreement except at 80 Hz where the difference of about 3% is due to the discretization error of the FE-PML approximation.

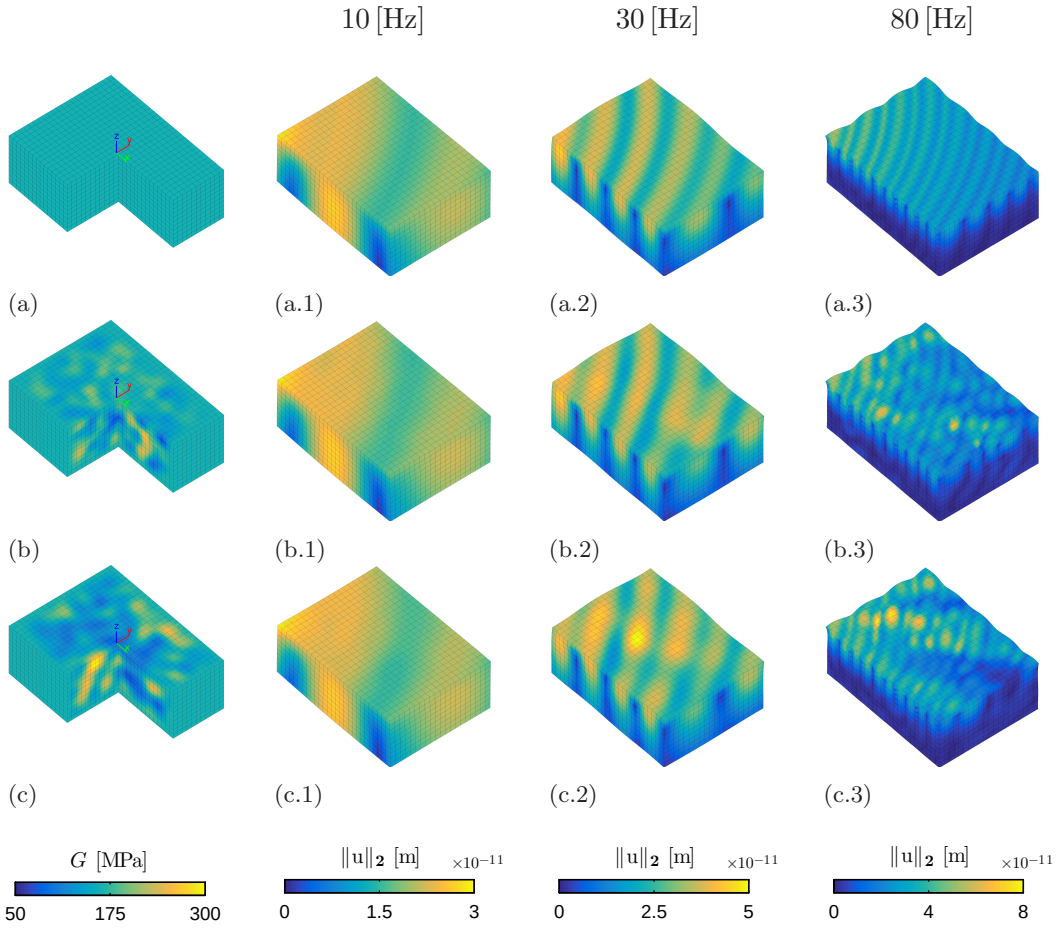

Figure 10: Realizations of the random field representing the stochastic shear modulus of the subsoil and snapshots of the corresponding free field displacements $\mathrm{u}(t) = |\hat{\mathrm{u}}| \cos(\omega t + \theta)$ at 10 Hz, 30 Hz and 80 Hz at $t = 0$ s. (a) Homogeneous subsoil with the mean properties of table 2, (b) random field with $l_\mathrm{c} = 1$ m and (c) random field with $l_\mathrm{c} = 1.5$ m.

5.3. Loading cases

In order to understand how the uncertain local subsoil conditions affect the structural response to ground-borne vibration, two loading cases are considered. The first loading case (LC1) is the solution of the problem where the incident wave field propagates through $\bar{\Omega}^\mathrm{e}_\mathrm{s}$ before it impinges the

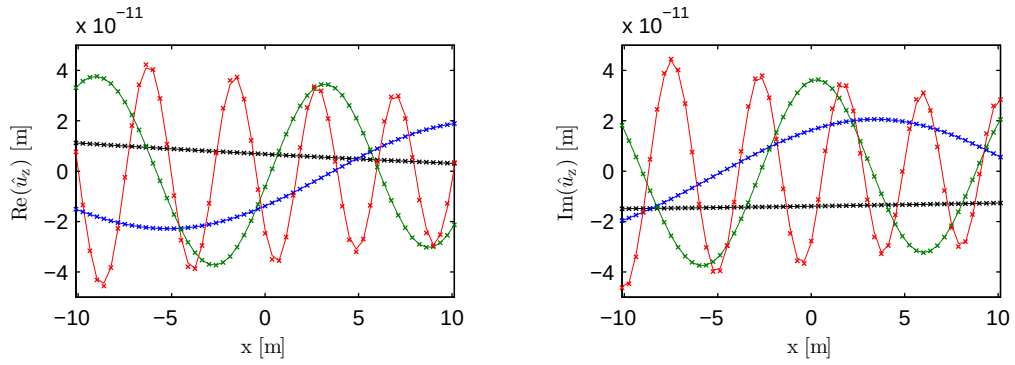

(a) (b)

Figure 11: (a) Real and (b) imaginary part of the free field vertical displacement $\hat{u}_z$ along the x-axis ($y = 0$, $z = 0$) of the FE-PML model (solid lines) in comparison with the direct stiffness method ($\times$ marks) at 1 Hz (black line), 10 Hz (blue line), 30 Hz (green line) and 80 Hz (red line).

foundation of the building. This loading case allows to assess the overall influence of the uncertain local subsoil conditions on the response of the building. Figures 12 and 13 demonstrate how the incident wave field (figure 10) is perturbed by the building. At low frequencies, the size of the building is small relative to the wavelength and the building does not perturb significantly the displacement field of the soil. However, at higher frequencies the building acts as a surface wave barrier significantly affecting the displacement field of the soil. This is more evident in the case of the building with raft foundation. Figures 10b-10c, 12b-12c and 13b-13c show how the impedance contrasts due to the randomly heterogeneous subsoil properties lead to constructive and destructive wave interference perturbing the displacement field of the soil.

In the second loading case (LC2), the excitation due to the incident wave field is applied as nodal forces directly on the soil-foundation interface Σ_{bs} assuming that the incident wave field has propagated through the subsoil with the deterministic properties of table 2, unperturbed by the uncertain local subsoil conditions. Figure 14 shows the displacement field $\hat{\mathbf{u}}_{\mathrm{sc}}$ radiated by the building in the soil due to the LC2. This loading case provides additional insight isolating the influence of the uncertain dynamic stiffness of the coupled soil-structure system on the response of the building.

5.4. Sensitivity analysis

For practical reasons, the volume of subsoil $\bar{\Omega}_{\mathrm{s}}^{\mathrm{e}}$ with imperfectly known properties is bounded to the vicinity of the building. In order to identify the volume of soil predominantly influencing the dynamic stiffness of the coupled soil-structure system, the sensitivity of the building response is computed with respect to the element-wise defined shear moduli of the soil in $\bar{\Omega}_{\mathrm{s}}^{\mathrm{e}}$ for the LC2 (figure 14). Differentiation of equation (34) with respect to the shear modulus G_j of element j of $\bar{\Omega}_{\mathrm{s}}^{\mathrm{e}}$ yields:

$$\frac{\partial \underline{\hat{\mathbf{u}}}}{\partial G_j} = -\hat{\mathbf{S}}^{-1} \frac{\partial \hat{\mathbf{S}}}{\partial G_j} \underline{\hat{\mathbf{u}}} \tag{50}$$

Normally, the volume of subsoil influencing the dynamic stiffness of the coupled soil-structure system is as large as required to fully attenuate the scattered displacement field $\hat{\mathbf{u}}_{\mathrm{sc}}$ (figure 14).

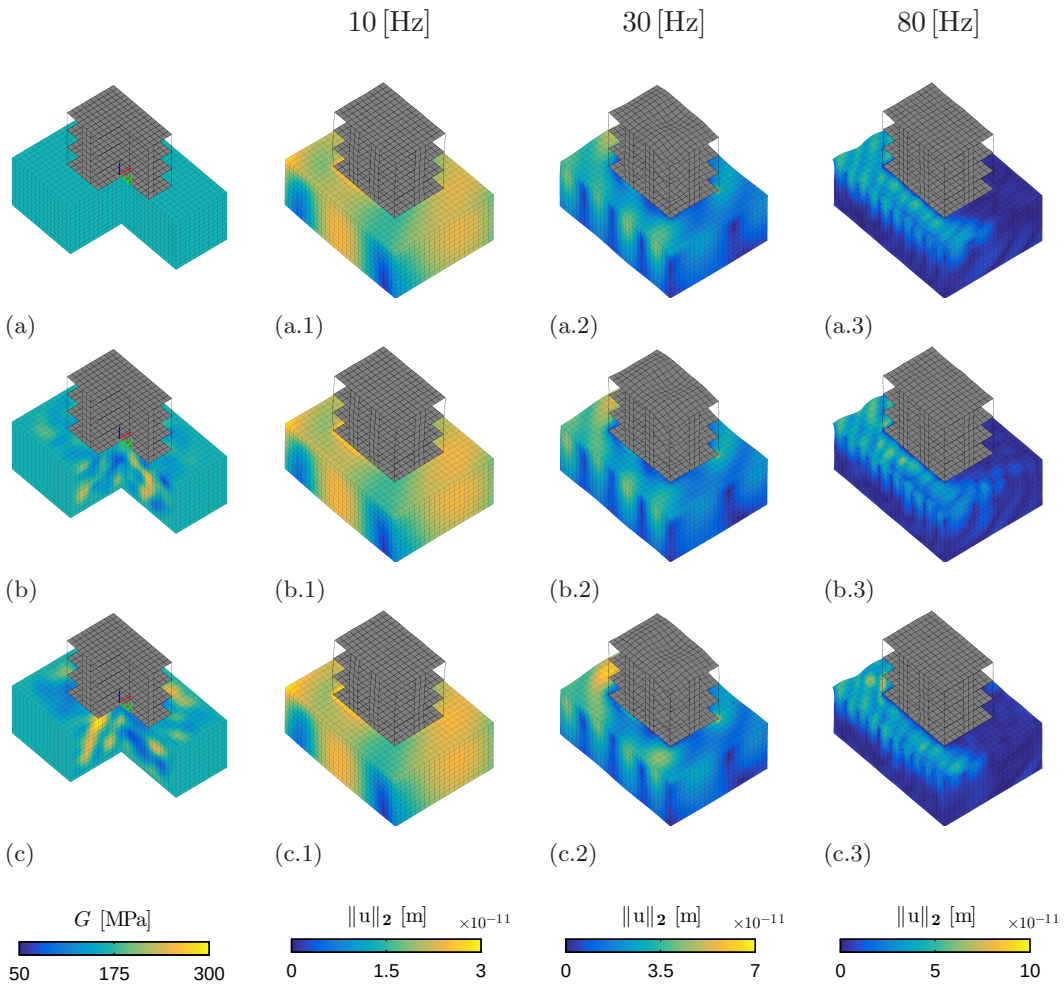

Figure 12: Realizations of the random field representing the stochastic shear modulus of the subsoil and snapshots of the corresponding displacements $\mathrm{u}(t) = |\hat{\mathrm{u}}| \cos(\omega t + \theta)$ of the building with raft foundation at 10 Hz, 30 Hz and 80 Hz at $t = 0$ s due to the LC1. (a) Homogeneous subsoil with the mean properties of table 2, (b) random field with $l_\mathrm{c} = 1$ m and (c) random field with $l_\mathrm{c} = 1.5$ m.

Practically however, a much smaller volume of subsoil is able to capture the predominant influence of the uncertain subsoil properties on the dynamic stiffness of the coupled soil-structure system.

Figure 15 shows the sensitivity of the vertical displacement at receiver R_1 (figure 7) with respect to the element-wise defined shear moduli of $\bar{\Omega}_\mathrm{s}^\mathrm{e}$ for a set of frequencies. The volume of subsoil that influences the response of R_1 changes with the frequency. At low frequencies, the wavelength is large compared to the size of the foundations (figures 14a.1 and 14b.1) and the local variation of the subsoil properties is not resolved in the response. The response of the building is sensitive only to the properties of a limited volume of subsoil which essentially contributes to the static stiffness of the foundations (figures 15a.1 and 15b.1). As the wavelength gets smaller at higher frequencies (figures 14a.2-14a.3 and 14b.2-14b.3), a larger volume of subsoil influences the response of R_1 (figures 15a.2-15a.3 and 15b.2-15b.3). This is more pronounced for the building with individual footings. The volume of subsoil predominantly contributing to the response of R_1 is generally

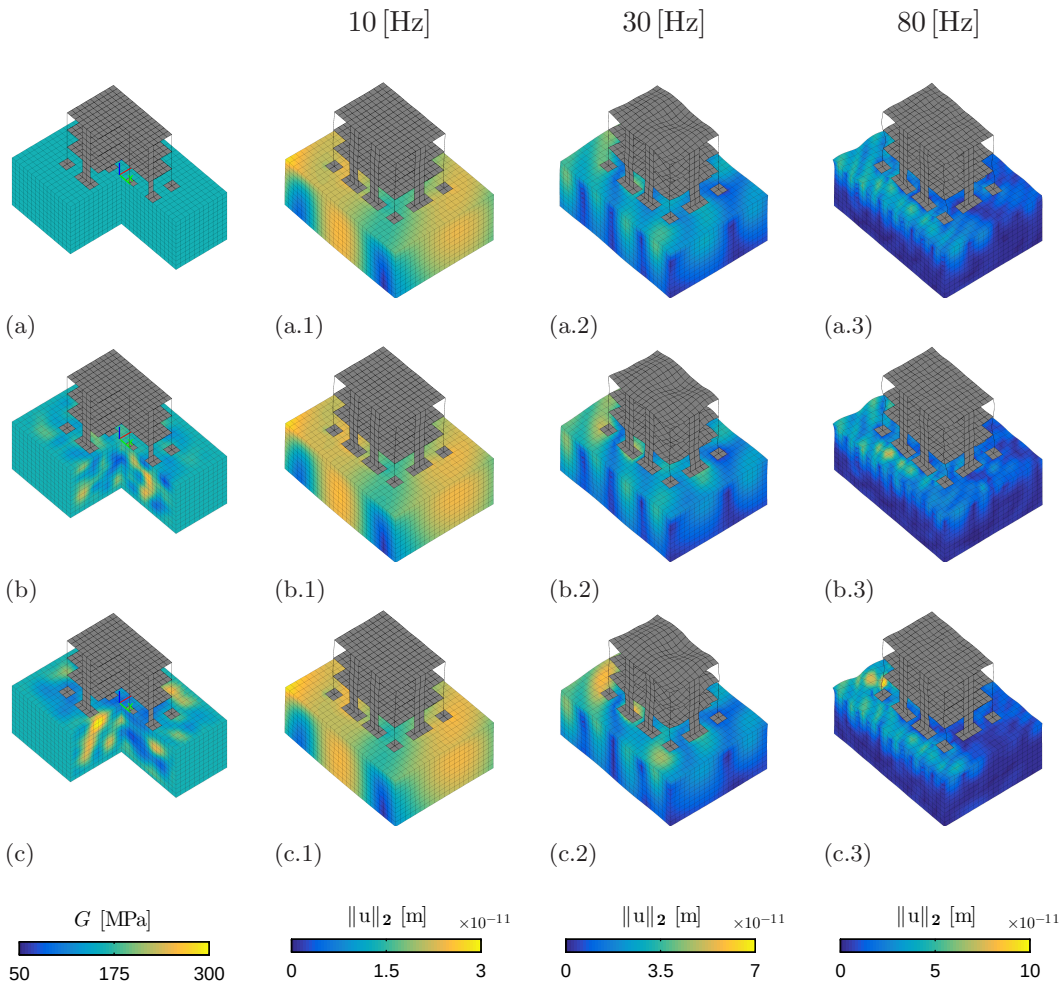

Figure 13: Realizations of the random field representing the stochastic shear modulus of the subsoil and snapshots of the corresponding displacements $\mathrm{u}(t) = |\hat{\mathrm{u}}| \cos(\omega t + \theta)$ of the building with individual footings at 10 Hz, 30 Hz and 80 Hz at $t = 0$ s due to the LC1. (a) Homogeneous subsoil with the mean properties of table 2, (b) random field with $l_\mathrm{c} = 1$ m and (c) random field with $l_\mathrm{c} = 1.5$ m.

larger at frequencies for which the subsoil is significantly mobilized by the bending modes of the floors (figures 14a.2 and 14b.2).

Apart from the dynamic stiffness of the coupled soil-structure system, the stochastic subsoil properties also influence the incident wave field exciting the building. In order to fully take this influence into account, the subdomain $\bar{\Omega}_\mathrm{s}^\mathrm{e}$ would have to extend to infinity which is computationally unfeasible with the present methodology. A pragmatic approach is to consider this influence in an average sense using effective elastic properties for the subsoil in the far field [44].

5.5. Propagation of uncertainty

The uncertainty is propagated from the subsoil properties to the building displacement transfer functions by means of Monte-Carlo simulation. In total, $n_\mathrm{R} = 1000$ realizations are used to estimate the uncertainty on the building response. The uncertainty is quantified by computing the coefficient

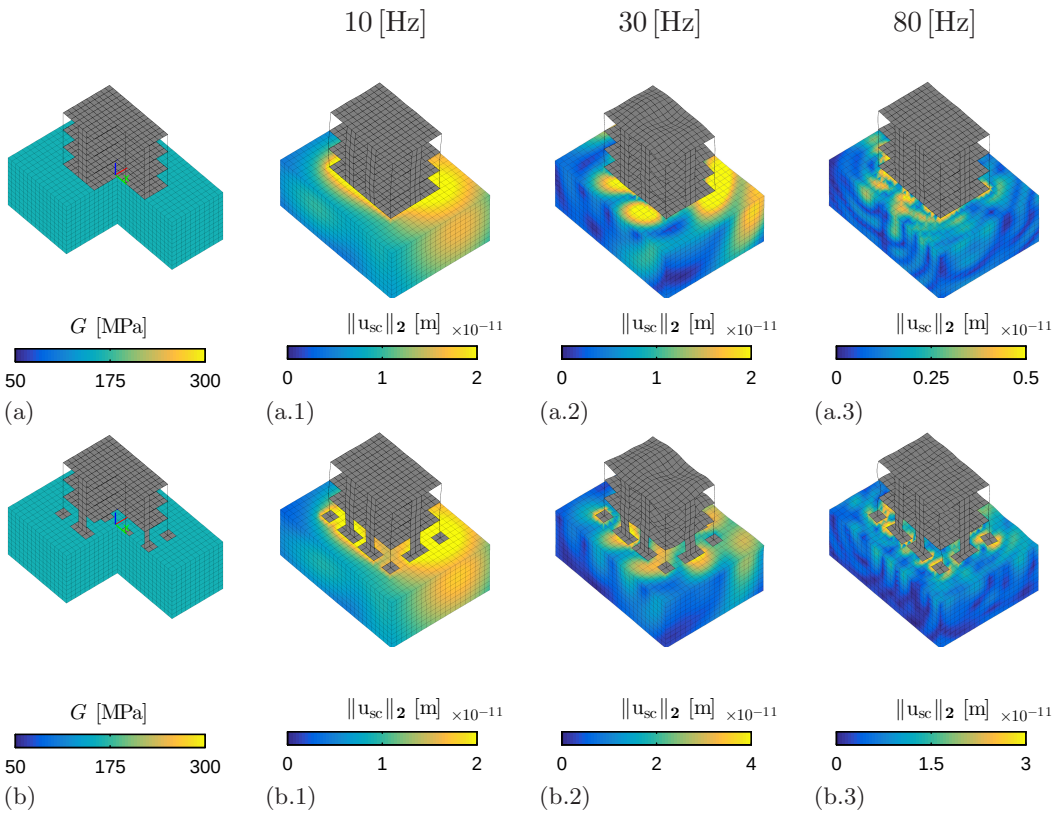

Figure 14: Snapshots of the displacements $u(t) = |\hat{u}| \cos(\omega t + \theta)$ at 10 Hz, 30 Hz and 80 Hz at $t = 0$ s due to the LC2. Building with (a) raft foundation and (b) individual footings.

of variation (CoV) and by constructing confidence regions for the building response. The CoV is defined as:

$$\mathrm{CoV}_{|\hat{u}_j|} = \frac{\sigma_{|\hat{u}_j|}}{\mu_{|\hat{u}_j|}} \tag{51}$$

where $\sigma_{|\hat{u}_j|}$ and $\mu_{|\hat{u}_j|}$ are the standard deviation and the mean value of the displacement $|\hat{u}_j|$ of the j-th degree of freedom. Alternatively, the confidence region with a confidence level of $p_c = 90\%$ for the displacement $|\hat{u}_j|$ is defined such that:

$$P(|\hat{u}_j^{\mathrm{l}}| \leq |\hat{u}_j| \leq |\hat{u}_j^{\mathrm{u}}|) \geq p_c \tag{52}$$

where the lower $|\hat{u}_j^{\mathrm{l}}|$ and the upper $|\hat{u}_j^{\mathrm{u}}|$ bounds are the 5% and 95% percentiles of $|\hat{u}_j|$, respectively. By utilizing the bootstrap method [45], a confidence region can be also estimated for $\mathrm{CoV}_{|\hat{u}_j|}$.

5.6. Free field and foundation displacement transfer functions

Figure 16 shows the transfer functions of the vertical displacement at the receiver location F_0 (figure 7) for the free field, the building with raft foundation and the building with individual footings. The mean free field response increases with the frequency whereas the mean response at the foundation level of the building with raft foundation and the building with individual footings

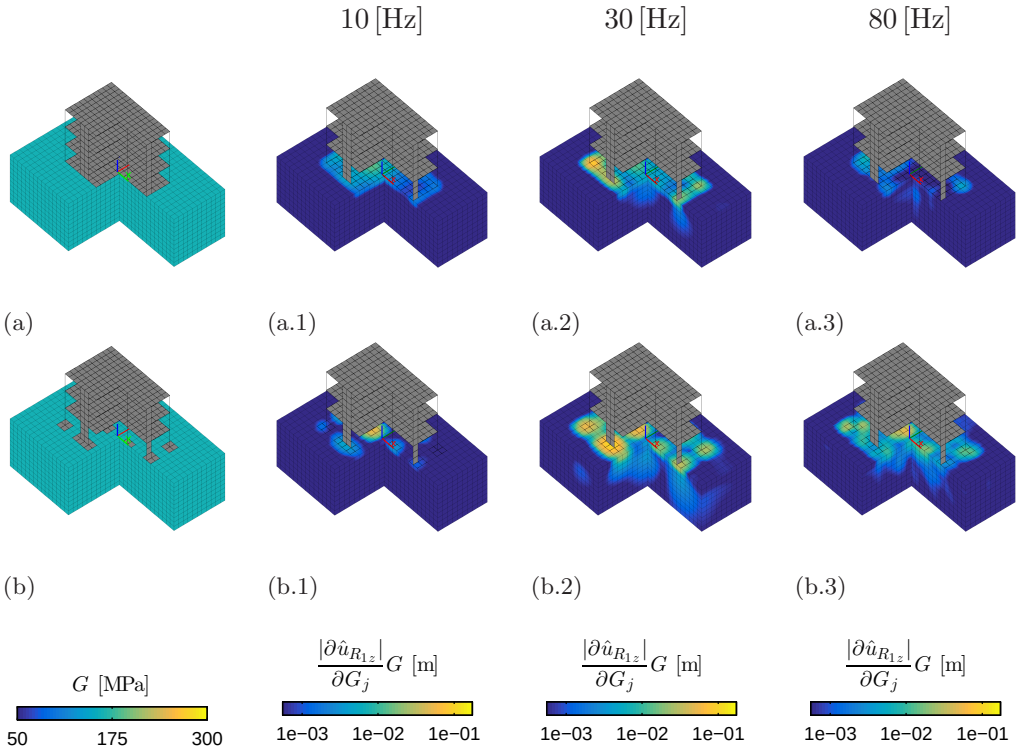

Figure 15: Vertical displacement sensitivity $|\frac{\partial \hat{u}}{\partial G_j}|G$ of receiver R_1 (figure 7) with respect to the element-wise defined shear moduli G_j of $\bar{\Omega}_{\mathrm{s}}^{\mathrm{e}}$ at 10 Hz, 30 Hz and 80 Hz. Building with (a) raft foundation and (b) individual footings.

shows resonance effects [6]. The mean response is significantly lower for the building with raft foundation for frequencies above 50 Hz. As the resonance peaks of the transfer functions occur at slightly different frequencies for each individual realization of the subsoil properties, this leads to mean transfer functions with smooth local maxima and minima. The mean transfer functions (figure 16a) are almost identical for the two correlation lengths $l_{\mathrm{c}} = 1\,\mathrm{m}$ and $l_{\mathrm{c}} = 1.5\,\mathrm{m}$ considered for the random field representing the shear modulus of the soil. The uncertainty bounds of the transfer functions (figure 16b) differ, however. The lower the correlation length l_{c}, the narrower the uncertainty bounds as the local scale variation of the shear modulus is averaged out in the response. The uncertainty of the free field vertical displacement at F_0 increases almost linearly with the frequency. Figures 10b and 10c demonstrate how the heterogeneous local subsoil conditions perturb the free field displacements more heavily as the frequency increases leading to higher uncertainty under imperfectly known subsoil conditions. The uncertainty of the building response follows a similar trend with the uncertainty of the free field response but the uncertainty increases sharply in the frequency ranges where the modulus of the mean transfer functions presents local minima.

5.7. Building displacement transfer functions

Figures 17-18 and 19-20 show the transfer functions of the horizontal and vertical displacements at the receiver locations R_1 and R_3, respectively, of the building with raft foundation and the building with individual footings (figure 7). The building response is higher in the vertical than

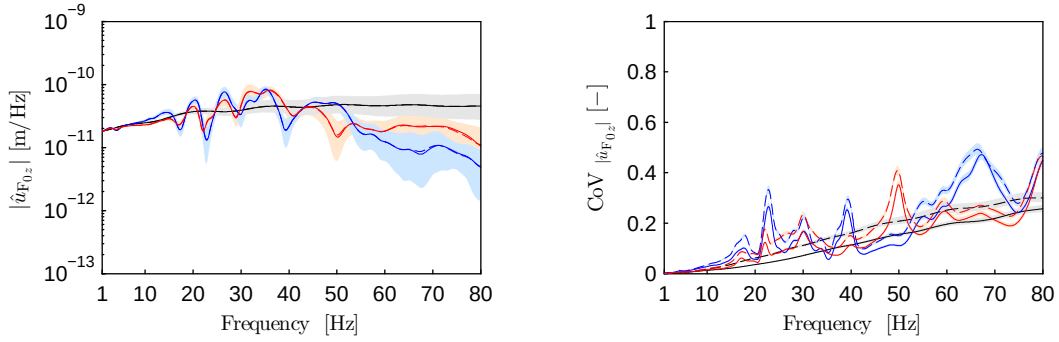

(a) (b)

Figure 16: (a) Mean and (b) CoV of the transfer function $|\hat{u}_{F_{0z}}|$ (figure 7) of the free field (black line), the building with raft foundation (blue line) and individual footings (red line) for $l_c = 1$ m (solid lines) and $l_c = 1.5$ m (dashed lines). The 90% confidence regions are shaded with the corresponding color.

in the lateral direction. The mean transfer functions of R_1 and R_3 (figures 17a-18a and 19a-20a, respectively) are approximately the same up to 15 Hz for the two buildings considered. At higher frequencies, the building with the stiffer raft foundation has lower response than the building with individual footings except near a few resonance frequencies.

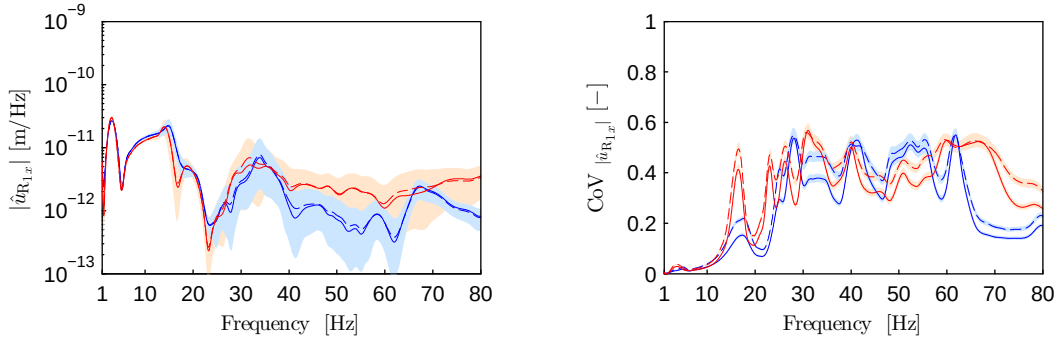

(a) (b)

Figure 17: (a) Mean and (b) CoV of the transfer function $|\hat{u}_{R_{1x}}|$ (figure 7) of the building with raft foundation (blue line) and individual footings (red line) for $l_c = 1$ m (solid lines) and $l_c = 1.5$ m (dashed lines). The 90% confidence regions are shaded with the corresponding color.

Similarly to the mean transfer functions of the free field and the foundations, the mean transfer functions of R_1 and R_3 differ slightly for the two correlation lengths considered for the random field representing the shear modulus of the soil. Again, the smaller correlation length results in narrower uncertainty bounds for the building response.In the frequency range up to 10 Hz, the response of both the building with raft foundation and the building with individual footings is almost deterministic (figures 17b-18b and 19b-20b, respectively) for the two correlation lengths considered. At higher frequencies, the uncertainty bounds of the transfer functions fluctuate significantly but the uncertainty retains a linear trend with respect to the frequency for the vertical displacements. The CoV of the lateral displacements ranges from 0.15 at 15 Hz to $0.35 - 0.60$ in the frequency

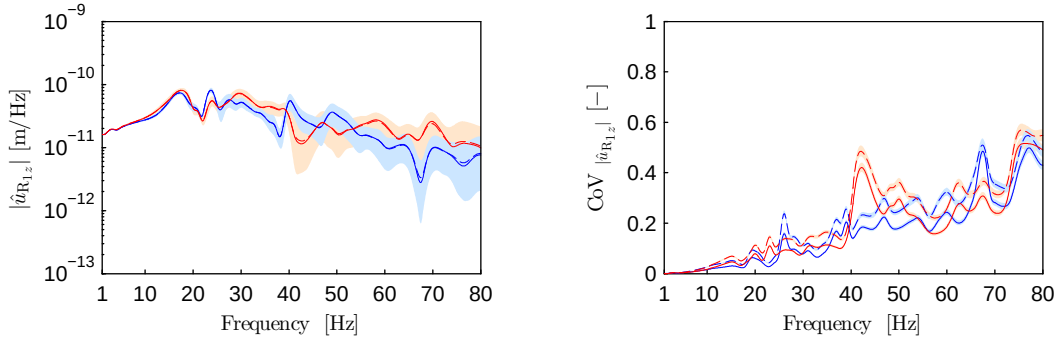

(a) (b)

Figure 18: (a) Mean and (b) CoV of the transfer function $|\hat{u}_{R_{1z}}|$ (figure 7) of the building with raft foundation (blue line) and individual footings (red line) for $l_c = 1$ m (solid lines) and $l_c = 1.5$ m (dashed lines). The 90% confidence regions are shaded with the corresponding color.

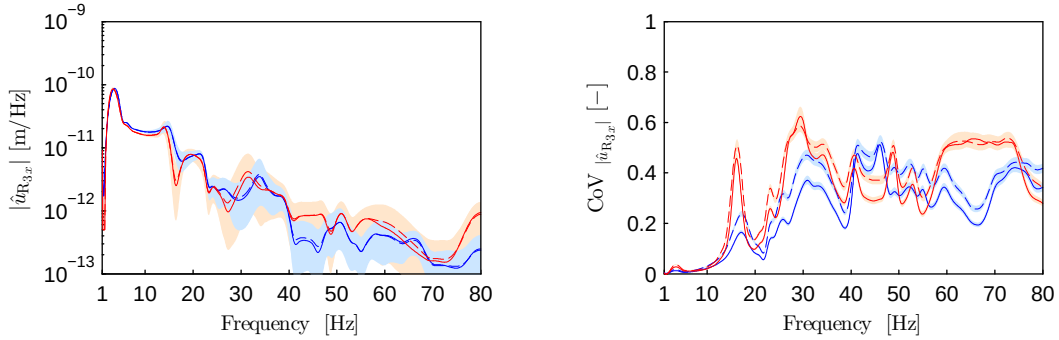

(a) (b)

Figure 19: (a) Mean and (b) CoV of the transfer function $|\hat{u}_{R_{3x}}|$ (figure 7) of the building with raft foundation (blue line) and individual footings (red line) for $l_c = 1$ m (solid lines) and $l_c = 1.5$ m (dashed lines). The 90% confidence regions are shaded with the corresponding color.

range between 30 and 80 Hz. The highest response uncertainty occurs in the frequency ranges where the modulus of the mean transfer functions shows local minima. In these frequency ranges, the CoV of the mean transfer functions is up to 2.5 times larger than the CoV of the soil's shear modulus.

5.8. Influence of the uncertain local subsoil conditions on the modal characteristics of the coupled soil-structure system

The imperfectly known local subsoil conditions result in uncertain dynamic stiffness, and corresponding modal characteristics, for the coupled soil-structure system and in an uncertain incident wave field exciting the building. Figures 21 and 22 show the transfer functions of the horizontal and vertical displacements at the receiver location R_1 of the building with raft foundation and the building with individual footings (figure 7) for LC2. Since a deterministic, unperturbed, incident wave field is considered in this loading case (section 5.3), the uncertainty on the building's transfer functions is only due to the uncertain modal characteristics of the coupled soil-structure system.

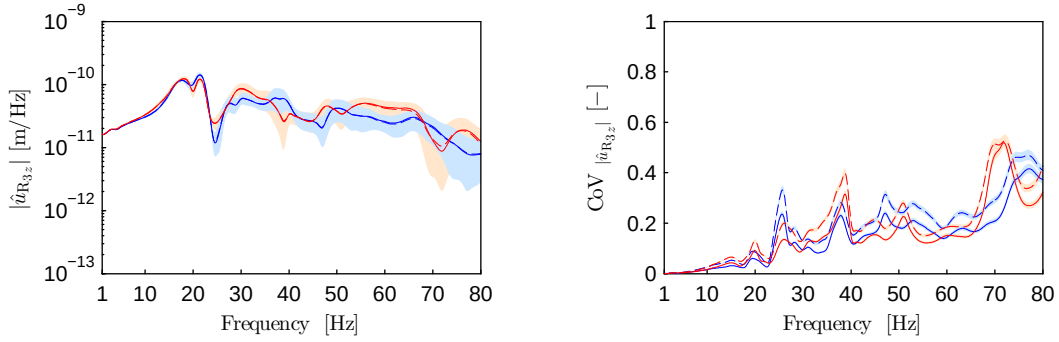

(a) (b)

Figure 20: (a) Mean and (b) CoV of the transfer function $|\hat{u}_{R_{3z}}|$ (figure 7) of the building with raft foundation (blue line) and individual footings (red line) for $l_c = 1$ m (solid lines) and $l_c = 1.5$ m (dashed lines). The 90% confidence regions are shaded with the corresponding color.

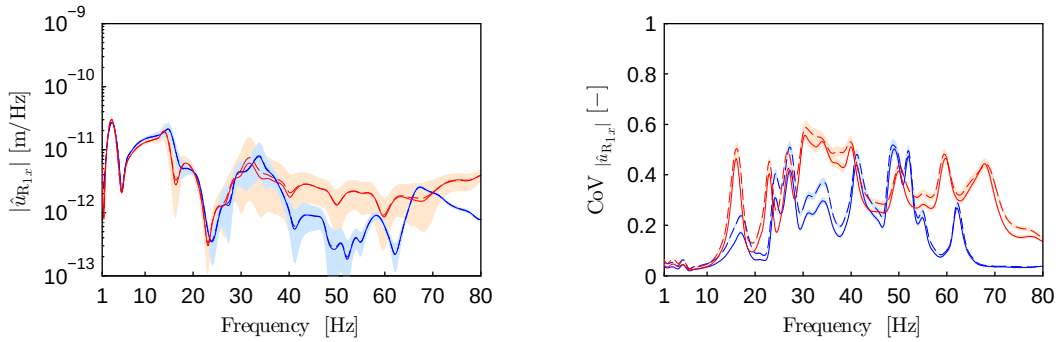

(a) (b)

Figure 21: (a) Mean and (b) CoV of the transfer function $|\hat{u}_{R_{1x}}|$ (figure 7) of the building with raft foundation (blue line) and individual footings (red line) for $l_c = 1$ m (solid lines) and $l_c = 1.5$ m (dashed lines) for LC2. The 90% confidence regions are shaded with the corresponding color.

The mean transfer functions of R_1 for LC2 (figures 21a and 22a) are similar to the mean transfer functions of R_1 for LC1 (figures 17a-18a). However, the associated uncertainty bounds for the vertical displacement (figure 22b) are narrower without following the linear trend observed in the uncertainty bounds for LC1 (figure 18b). Because the incident wave field excites the building mainly in the vertical direction, the lateral response of the building is less sensitive to the incident wave field. Comparison of figures 17 and 21 suggests that most of the uncertainty on the lateral response of the building is due to the uncertain modal characteristics of the coupled soil-structure system and to a lesser extent to the uncertain incident wave field.

The CoV of the vertical displacement of both the building with raft foundation and the building with individual footings does not fluctuate significantly in the frequency range up to 40 Hz lying around 0.15 (figure 22b). However, the CoV of the vertical displacement of the building with individual footings increases significantly at higher frequencies. Because the size of the individual footings is small compared to the scale of variation of the subsoil properties, each footing essentially

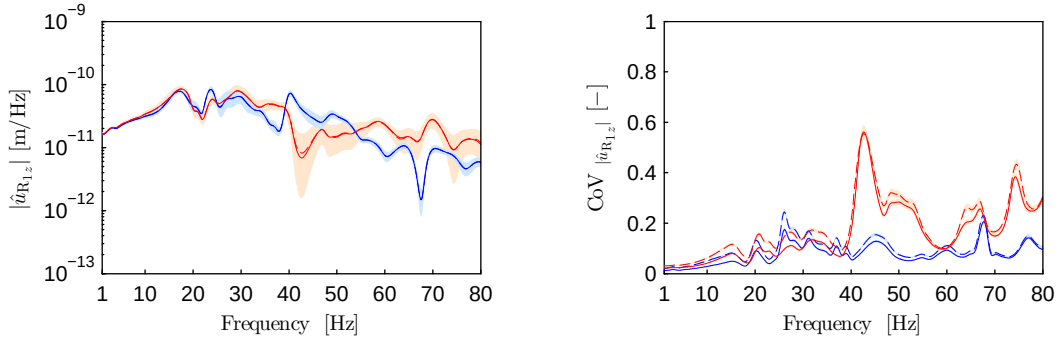

(a) (b)

Figure 22: (a) Mean and (b) CoV of the transfer function $|\hat{u}_{R_1z}|$ (figure 7) of the building with raft foundation (blue line) and individual footings (red line) for $l_c = 1$ m (solid lines) and $l_c = 1.5$ m (dashed lines) for LC2. The 90% confidence regions are shaded with the corresponding color.

rests on top of a soil with different properties (figure 13). As a result, the modal characteristics of the building with individual footings are more sensitive to the spatial variation of the soil properties than the modal characteristics of the building with raft foundation (figure 12).

The range of the uncertainty bounds of the building's transfer functions indicates that the influence of the uncertain local subsoil conditions on the modal characteristics of the coupled soil-structure system is negligible at low frequencies, but gets significant at higher frequencies. It is well known from earthquake engineering that the importance of dynamic SSI increases when the relative stiffness between the subsoil and the building decreases [2]. Although the mean stiffness of the subsoil is rather high (table 2), the uncertainty bounds of the building's transfer functions suggest that dynamic SSI can be important in the case of a heterogeneous subsoil when the scale of variation of the subsoil properties lies within the correlation lengths considered (figures 21b and 22b).

6. Conclusions

In this paper, the influence of imperfectly known local subsoil conditions on the response of buildings to environmental ground-borne vibration is examined. A FE-PML model is developed for the stochastic dynamic SSI problem where the shear modulus of the subsoil in the vicinity of the building is represented by a conditional random field. An external incident wave field is propagated through the FE-PML model using a subdomain formulation. The uncertainty on the subsoil properties is propagated to the building displacement transfer functions by means of Monte Carlo simulation. A case study is considered to investigate the influence of the spatial correlation length of the subsoil's shear modulus and the foundation type of the building on the structural response to ground vibration. A building with raft foundation and a building with individual footings are considered excited by an incident wave field generated by a vertical point load at the surface of the soil.

The imperfectly known local subsoil conditions influence the response of the building resulting in uncertain modal characteristics for the coupled soil-structure system and in an uncertain incident wave field. The two correlation lengths considered for the random field representing the shear

modulus of the soil give almost identical mean transfer functions for the response of the building. However, the uncertainty bounds of the transfer functions differ between the two cases with the shorter correlation length leading to slightly lower uncertainty bounds. As the incident wave field excites the building predominantly in the vertical direction, the vertical response of the building is particularly sensitive to the uncertain incident wave field with the vertical response uncertainty following a linear trend with respect to the frequency. The uncertainty on the lateral response of the building is mostly due to the uncertain modal characteristics of the coupled soil-structure system and to a lesser extent to the uncertain incident wave field. This uncertainty varies considerably over frequency bands.

The uncertainty on the micro-scale variability of the local subsoil conditions can be neglected for seismic SSI problems as the response in the frequency range up to 10 Hz is practically deterministic. The building response uncertainty increases significantly at higher frequencies being generally larger than the considered uncertainty on the soil's shear modulus. The uncertainty on the modal characteristics of the coupled soil-structure system shows that dynamic SSI can be important at higher frequencies in the case of randomly heterogeneous soils even if the mean soil stiffness is rather high. For reliable response predictions of buildings to environmental ground-borne vibration the uncertain local subsoil conditions should be taken into account. This requires additional laboratory and in situ tests to statistically characterize the subsoil properties at a fine spatial resolution, however.

Acknowledgments

The research presented in this paper was performed within the frame of the project OT/13/59 "Quantifying and reducing uncertainty in structural dynamics" funded by the Research Council of KU Leuven. The financial support is gratefully acknowledged.

References

[1] D. Beskos, T. Krauthammer, I. Vardoulakis (Eds.), Dynamic soil-structure interaction, A.A. Balkema, 1984.
[2] J. Wolf, Dynamic soil-structure interaction, Prentice-Hall, Englewood Cliffs, New Jersey, 1985.
[3] G. Mylonakis, C. Syngros, G. Gazetas, T. Tazoh, The role of soil in the collapse of 18 piers of Hanshin expressway in the Kobe earthquake, Earthquake Engineering and Structural Dynamics 35 (2006) 547–575.
[4] D. Clouteau, G. Degrande, G. Lombaert, Numerical modeling off traffic induced vibrations, Meccanica 36 (4) (2001) 401–420.
[5] P. Fiala, G. Degrande, F. Augusztinovicz, Numerical modelling of ground-borne noise and vibration in buildings due to surface rail traffic, Journal of Sound and Vibration 301 (2007) 718–738.
[6] S. François, L. Pyl, H. Masoumi, G. Degrande, The influence of dynamic soil-structure interaction on traffic induced vibrations in buildings, Soil Dynamics and Earthquake Engineering 27 (2007) 655–674.
[7] O. Von Estorff, E. Kausel, Coupling of boundary and finite-elements for soil-structure interaction problems, Earthquake Engineering and Structural Dynamics 18 (7) (1989) 1065–1075.
[8] J. Lysmer, R. Kuhlemeyer, Finite dynamic model for infinite media, Journal of the Engineering Mechanics Division 95 (EM4) (1969) 859–877.
[9] F. Medina, J. Penzien, Infinite elements for elastodynamics, Earthquake Engineering and Structural Dynamics 10 (5) (1982) 699–709.
[10] W. Chew, Q. Liu, Perfectly matched layers for elastodynamics: a new absorbing boundary condition, Journal of Computational Acoustics 4 (4) (1996) 341–359.
[11] U. Basu, A. Chopra, Perfectly matched layers for time-harmonic elastodynamics of unbounded domains: theory and finite-element implementation, Computer Methods in Applied Mechanics and Engineering 192 (11–12) (2003) 1337–1375.

[12] U. Basu, A. Chopra, Perfectly matched layers for transient elastodynamics of unbounded domains, International Journal for Numerical Methods in Engineering 59 (2004) 1039–1074.
[13] D. Aubry, D. Clouteau, A subdomain approach to dynamic soil-structure interaction, in: V. Davidovici, R. Clough (Eds.), Recent advances in earthquake engineering and structural dynamics, Nantes: OUEST Editions/AFPS, 1992, pp. 251–272.
[14] E. Kausel, J. Roësset, Stiffness matrices for layered soils 71 (6) (1981) 1743–1761.
[15] E. Kausel, Fundamental Solutions in Elastodynamics: A Compendium, Cambridge University Press, 2006.
[16] G. Baecher, J. Christian, Reliability and Statistics in Geotechnical Engineering, Wiley & Sons, 2003.
[17] E. Savin, D. Clouteau, Elastic wave propagation in a 3D unbounded random heterogeneous medium coupled with a bounded medium. application to seismic soil-structure interaction (SSSI), International Journal for Numerical Methods in Engineering 54 (2002) 607–630.
[18] D. Ghiocel, R. Ghanem, Stochastic finite-element analysis of seismic soil-structure interaction, Journal of Engineering Mechanics 128 (2002) 66–77.
[19] E. Vanmarcke, Random Fields: Analysis and Synthesis, MIT Press Classics, 1983.
[20] C. Soize, A non-parametric model of random uncertainties for reduced matrix models in structural dynamics, Probabilistic Engineering Mechanics 15 (3) (2000) 277–294.
[21] R. Cottereau, D. Clouteau, C. Soize, S. Cambier, Probabilistic nonparametric model of impedance matrices. Application to the seismic design of a structure, European Journal of Computational Mechanics 15 (1-2-3) (2006) 131–142.
[22] M. Arnst, D. Clouteau, H. Chebli, R. Othman, G. Degrande, A non-parametric probabilistic model for ground-borne vibrations in buildings, Probabilistic Engineering Mechanics 21 (2006) 18–34.
[23] P. Ropars, G. Bonnet, P. Jean, stabilization process applied to a hidden variables method for evaluating the uncertainties on foundation impedances and their effect on vibrations induced by railways in a building, Journal of Sound and Vibration 333 (2014) 1953–1971.
[24] M. Papadopoulos, S. François, G. Degrande, G. Lombaert, Analysis of stochastic dynamic soil-structure interaction problems by means of coupled finite elements-perfectly matched layers, Proceedings of the European Congress on Computational Methods in Applied Sciences and Engineering 2016, Crete, Greece, 2016, pp. 6172–6185.
[25] A. Eringen, E. Suhubi, Elastodynamics, Volume 2, Linear theory, Academic Press, New York, USA, 1975.
[26] P. Coulier, S. François, G. Degrande, G. Lombaert, The influence of source-receiver interaction on the numerical prediction of traffic induced vibrations, Journal of Sound and Vibration 333 (12) (2014) 81–86.
[27] M. Schevenels, S. François, G. Degrande, EDT: An elastodynamics toolbox for MATLAB, Computers & Geosciences 35 (8) (2003) 1752–1754.
[28] W. Chew, J. Jin, E. Michielssen, Complex coordinate stretching as a generalized absorbing boundary condition, Microwave and Optical Technology Letters 15 (6) (1997) 363–369.
[29] S. Kucukcoban, L. Kallivokas, A symmetric hybrid formulation for transient wave simulations in pml-truncated heterogeneous media, Wave Motion 50 (2013) 57–79.
[30] A. Tarantola, Inverse Problem Theory and Methods for Model Parameter Estimation, SIAM, 2005.
[31] W. Puła, J. Bauer, Application of the response surface method, in: D. Griffiths, G. Fenton (Eds.), Probabilistic methods in geotechnical engineering, CISM Courses and lectures, Vol. 491, 2007, pp. 147–168.
[32] P. Mayne, G. Rix, Correlations between shear wave velocity and cone tip resistance in natural clays, Soils and Foundations 35 (2) (1995) 107–110.
[33] M. Huber, Soil variability and its consequences in geotechnical engineering, Ph.D. thesis, Institut für Geotechnik der Universität Stuttgart (2013).
[34] C. Soize, Construction of probability distributions in high dimensions using the maximum entropy principle: applications to stochastic processes, random fields and random matrices, International Journal for Numerical Methods in Engineering 75 (2008) 1583–1611.
[35] M. Arnst, Inversion of probabilistic models of structures using measured transfer functions, Ph.D. thesis, Ecole Centrale Paris (2007).
[36] C. Li, A. Der Kiureghian, Optimal discretization of random fields, Journal of Engineering Mechanics 119 (6) (1993) 1136–1154.
[37] P. Liu, D. K. A., Multivariate distribution models with prescribed marginals and covariances, Probabilistic Engineering Mechanics 1 (2) (1986) 105–112.
[38] A. Olsson, G. Sandberg, Latin hypercube sampling for stochastic finite element analysis, technical notes, Journal of Engineering Mechanics 128 (2002) 121–125.
[39] M. Santare, P. Thamburaj, G. Gazonas, The use of graded finite elements in the study of elastic wave propagation

in continuously nonhomogeneous materials, International Journal of Solids and Structures 40 (2003) 5621–5634.
[40] W. Read, Stress analysis for compressible viscoelastic materials 21 (1950) 671–674.
[41] F. Rizzo, D. Shippy, An application of the correspondence principle of linear viscoelasticity theory, SIAM Journal on Applied Mathematics 21 (2) (1971) 321–330.
[42] R. Clough, J. Penzien, Dynamics of structures, McGraw-Hill, 1975.
[43] S. François, M. Schevenels, G. Lombaert, G. Degrande, A two-and-a-half-dimensional displacement-based pml for elastodynamic wave propagation, International Journal for Numerical Methods in Engineering 90 (2012) 819–837.
[44] D. Clouteau, R. Cottereau, G. Lombaert, Dynamics of structures coupled with elastic media - A review of numerical models and methods, Journal of Sound and Vibration 332 (2013) 2415–2436.
[45] B. Efron, R. Tibshirani, An Introduction to the Bootstrap, Chapman & Hall, 1993.